

Kinetic energy dissipation and fluctuations in strongly-damped heavy-ion collisions within the stochastic mean-field approach

Sakir Ayik^{1,*} and Kazuyuki Sekizawa^{2,3,†}

¹*Physics Department, Tennessee Technological University, Cookeville, Tennessee 38505, USA*

²*Center for Transdisciplinary Research, Institute for Research Promotion, Niigata University, Niigata 950-2181, Japan*

³*Division of Nuclear Physics, Center for Computational Sciences, University of Tsukuba, Ibaraki 305-8577, Japan*

(Dated: December 23, 2020)

Background: Microscopic mean-field approaches have been successful in describing the most probable reaction outcomes in low-energy heavy-ion reactions. However, those approaches are known to severely underestimate dispersions of observables around the average values that has limited their applicability. Recently it has been shown that a quantal transport approach based on the stochastic mean-field (SMF) theory significantly improves the description, while its application has been limited so far to fragment mass and charge dispersions.

Purpose: In this work, we extend the quantal transport approach based on the SMF theory for relative kinetic energy dissipation and angular momentum transfer in low-energy heavy-ion reactions.

Methods: Based on the SMF concept, analytical expressions are derived for the radial and tangential friction and associated diffusion coefficients. Those quantal transport coefficients are calculated microscopically in terms of single-particle orbitals within the time-dependent Hartree-Fock (TDHF) approach.

Results: As the first application of the proposed formalism, we consider the radial linear momentum dispersion, neglecting the coupling between radial and angular momenta. We analyze the total kinetic energy (TKE) distribution of binary reaction products in the $^{136}\text{Xe}+^{208}\text{Pb}$ reaction at $E_{c.m.} = 526$ MeV and compare with experimental data. From time evolution of single-particle orbitals in TDHF, the radial diffusion coefficient is computed on a microscopic basis, while a phenomenological treatment is introduced for the radial friction coefficient. By solving the quantal diffusion equation for the radial linear momentum, the dispersion of the radial linear momentum is obtained, from which one can construct the TKE distribution. We find that the calculations provide a good description of the TKE distribution for strongly-damped events with large energy losses, $\text{TKEL} \gtrsim 150$ MeV. However, the calculations underestimate the TKE distribution for smaller energy losses. Further studies are needed to improve the technical details of calculations.

Conclusions: It has been shown that the quantal transport approach based on the SMF theory provides a promising basis for the microscopic description of the TKE distribution as well as the isotopic distributions in damped collisions of heavy ions at around the Coulomb barrier.

I. INTRODUCTION

The nuclear dissipation plays a major role in nuclear dynamics such as heavy-ion collisions as well as nuclear fission. In order to understand the nuclear dissipation mechanism, a large amount of investigations have been carried out both experimentally and theoretically over many years [1–4]. In low-energy heavy-ion collisions at around the Coulomb barrier, the one-body dissipation-fluctuation mechanism originating from nucleon exchange is essential. The time-dependent Hartree-Fock (TDHF) approach provides a microscopic basis for describing dissipative collisions at low energies. It incorporates with the one-body dissipation mechanism and successfully describes the most probable dynamical path of reaction dynamics [5–11]. However, it is well known that the mean-field treatment of the TDHF approach severely underestimates dynamical fluctuations around the most probable path. Recent applications of the so-called time-dependent random phase approximation (TDRPA), which is based on the generalized variational principle of Balian and Vénéroni [12–14], provides a possible prescription for calculating dispersions of one-body observables in low-energy heavy-ion reactions. The latter ap-

proach has been applied to calculate mass and charge dispersions in heavy-ion collisions [15–18]. Although there was an attempt to quantify kinetic energy fluctuations in dissipative collisions in the past [19], its practical applications are still scarce. This work is the first step toward the fully microscopic description of dissipation and fluctuations of the relative motion of colliding nuclei based on an alternative approach, the stochastic mean-field (SMF) theory [20, 21].

It is crucially important to develop a microscopic basis for describing fluctuations in the kinetic energy dissipation for providing a reliable prediction for producing unknown unstable nuclei. In recent years, deep-inelastic collisions such as multinucleon transfer and quasifission processes have engaged substantial interests, regarding the possibility of efficient production of unknown neutron-rich heavy nuclei. Production of transactinide nuclei in the superheavy region in deep-inelastic or quasifission type processes in damped collisions of two heavy nuclei has been explored. Besides, multinucleon transfer reactions at energies around the Coulomb barrier are expected to be useful to produce neutron-rich heavy nuclei along the neutron magic number $N = 126$. (See, e.g., Refs. [22, 23], for recent reviews.) To provide a reliable prediction for production of yet-unknown unstable nuclei, it is of paramount importance to properly describe not only dispersions of mass and charge of reaction products, as was greatly improved by the recent developments of the SMF approach [24–31], but also the distribution of dissipated relative kinetic

* ayik@tntech.edu

† sekizawa@phys.sc.niigata-u.ac.jp

energy during the collision. The latter is directly connected with excitation energies of reaction products, which should not be too large to maximize the production yield. Regarding the ongoing worldwide experimental effort aiming at producing unknown neutron-rich heavy nuclei [23, 33–40], it is an imperative task to develop a fully microscopic framework for dissipation and fluctuations of the relative motion of colliding nuclei associated with nucleon exchange.

In this work, we develop a quantal transport formalism for dissipation and fluctuations of the relative kinetic energy and the relative angular momentum transfer based on the SMF approach. Analytical expressions for the radial and tangential friction and associated diffusion coefficients are derived on the microscopic basis. As a first step toward the fully microscopic description of energy and angular momentum dissipation in low-energy heavy-ion reactions, in the present work, we consider dissipation of the relative radial linear momentum, neglecting its coupling with the angular momentum transfer. The kinetic energy dissipation in the collision of $^{136}\text{Xe}+^{208}\text{Pb}$ at $E_{c.m.} = 526$ MeV is analyzed with the newly developed approach and the total kinetic energy (TKE) distribution is compared with the available experimental data [33].

The article is organized as follows. In Sec. II, we present derivation of the Langevin equations for the relative radial momentum and the orbital angular momentum. In Sec. III, quantal expressions of diffusion coefficients for the radial and angular momenta, and the joint probability distribution function for these quantities are given. In Sec. IV, the numerical results of the TKE distribution for the $^{136}\text{Xe}+^{208}\text{Pb}$ reaction at $E_{c.m.} = 526$ MeV are presented and compared with the experimental data. A summary and conclusions are given in Sec. V.

II. FLUCTUATION OF THE RELATIVE MOMENTA WITHIN THE SMF APPROACH

A. Remarks on the SMF approach

The SMF approach goes beyond the standard TDHF description and provides a microscopic basis for describing the fluctuations around the most probable path [20, 21]. In the SMF approach, instead of a single deterministic event in TDHF, an ensemble of mean-field events is considered, which is associated with a distribution law. The single-particle density matrix of an event λ is given by

$$\rho^\lambda(\mathbf{r}, \mathbf{r}', t) = \sum_{ij} \phi_{ij}^*(\mathbf{r}, t; \lambda) \rho_{ij}^\lambda \phi_{ij}(\mathbf{r}', t; \lambda), \quad (1)$$

where the wave functions in each event λ obey the TDHF equation under own self-consistent mean field of the event. According to the basic postulate of the SMF approach, elements of the density matrix ρ_{ij}^λ at the initial state have uncorrelated Gaussian distribution with the average values $\overline{\rho_{ij}^\lambda} = n_j \delta_{ji}$ and the variances determined according to

$$\overline{\delta \rho_{ij}^\lambda \delta \rho_{i'j'}^\lambda} = \frac{1}{2} [n_j(1 - n_i) + n_i(1 - n_j)] \delta_{jj'} \delta_{ii'}, \quad (2)$$

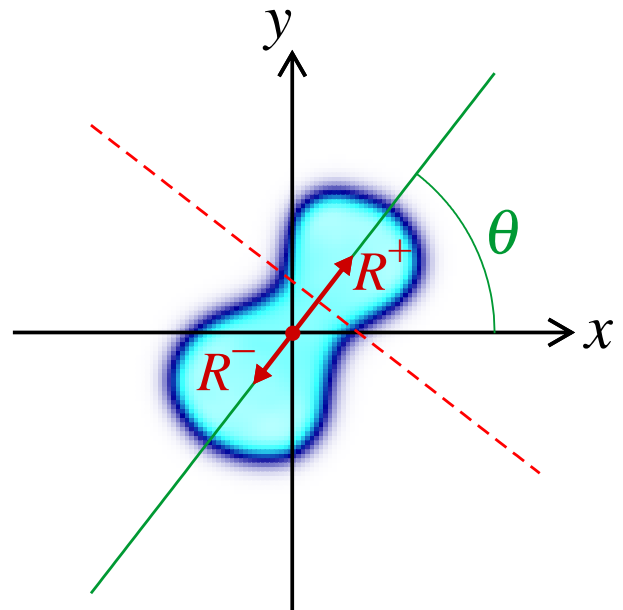


FIG. 1. Density profile in the reaction plane at a certain instant in the $^{136}\text{Xe}+^{208}\text{Pb}$ reaction at $E_{c.m.} = 526$ MeV with initial orbital angular momentum of $l = 200\hbar$. The beam direction is parallel to the $-x$ direction and the impact parameter vector is parallel to $+y$ direction. The orientation angle of the dinuclear system is indicated by θ ($= 52.2^\circ$ at this instant). The red dot represents the center of mass position of the system. The position vectors of projectile-like and target-like fragments in the center-of-mass frame are indicated by \mathbf{R}^+ and \mathbf{R}^- , respectively, where the relative distance at this instant is $R = |\mathbf{R}^+ - \mathbf{R}^-| = 13.7$ fm. The dashed line indicates the position of the window plane placed at the minimum density location.

where $\delta \rho_{ij}^\lambda = \rho_{ij}^\lambda - n_j \delta_{ji}$ and n_j denotes the average occupation numbers of the single particle states. Here and hereafter, the bar over quantities represents the ensemble average over the stochastically generated events. At zero temperature the occupation numbers are zero or one, while at finite temperatures they are specified according to the Fermi-Dirac distribution. The distribution law (2) ensures that an ensemble average of observables recovers the quantal expressions for the mean and the variance at the initial state.

In the special case, where colliding nuclei maintain a dinuclear structure (cf. Fig. 1, showing a typical density distribution in the $^{136}\text{Xe}+^{208}\text{Pb}$ reaction to be analyzed in Sec. IV), it is possible to analyze reaction dynamics in terms of a few macroscopic variables, such as relative linear and angular momenta, and mass and charge asymmetries of the dinuclear system. In this case, the SMF approach gives rise to a set of coupled Langevin equations for the macroscopic variables, which provides a quantal diffusion description of complex reaction dynamics in terms of a few relevant macroscopic variables. With the quantal diffusion equations, one can calculate not only the mean values of observables, which coincide with the TDHF results, but also distributions of the observables. For details of the SMF approach we refer readers to Refs. [20, 21, 25, 26]. We also refer to recent applications of the SMF approach for the multinucleon transfer mechanism in the dissipation heavy-ion collisions in Refs. [24–31] and

for kinetic energy fluctuations in spontaneous fission [32].

B. Rate of change of the relative linear momentum

In this section, let us recall basic equations that characterize the relative motion of colliding nuclei. We define the relative distance, $\mathbf{R}(t)$, the reduced mass, $\mu(t)$, and the relative linear momentum, $\mathbf{P}(t)$, in terms of the TDHF solutions with the help of the window dynamics, see Fig. 1. Figure 1 illustrates the elongation axis (the solid line) and the window plane (the dashed line) at a certain instant in the $^{136}\text{Xe}+^{208}\text{Pb}$ reaction at $E_{\text{c.m.}} = 526 \text{ MeV}$ with the initial orbital angular momentum $l = 200\hbar$. The orientation angle is indicated by θ in the reaction plane. The elongation axis of the dinuclear system can be determined by diagonalizing the mass quadrupole tensor at any instant. The window plane is perpendicular to the elongation axis and passes through the minimum density location on the elongation axis. For description of the details of the window dynamics we refer to Appendix A in Ref. [26].

In Fig. 1, the position vectors pointing the mean center-of-mass position of projectile- and target-like fragments in the center-of-mass frame are indicated by \mathbf{R}^+ and \mathbf{R}^- , respectively. In terms of the local density ρ_λ and the current density \mathbf{j}_λ in the event λ , the masses, the center-of-mass positions, and the linear momenta of the projectile- and target-like fragments are, respectively, given by

$$M_\lambda^\pm(t) = m \int d\mathbf{r} \Theta(\pm x') \rho_\lambda(\mathbf{r}, t), \quad (3)$$

$$\mathbf{R}_\lambda^\pm(t) = m \int d\mathbf{r} \Theta(\pm x') \mathbf{r} \rho_\lambda(\mathbf{r}, t) / M_\lambda^\pm(t), \quad (4)$$

$$\mathbf{P}_\lambda^\pm(t) = m \int d\mathbf{r} \Theta(\pm x') \mathbf{j}_\lambda(\mathbf{r}, t), \quad (5)$$

where \mathbf{j}_λ denotes the current density in the event λ ,

$$\mathbf{j}_\lambda(\mathbf{r}, t) = \frac{\hbar}{2mi} \sum_{ij} \left[\phi_j^*(\mathbf{r}, t; \lambda) \nabla \phi_i(\mathbf{r}, t; \lambda) - \phi_i(\mathbf{r}, t; \lambda) \nabla \phi_j^*(\mathbf{r}, t; \lambda) \right] \rho_{ji}^\lambda. \quad (6)$$

In Eqs. (3)–(5) we neglect the fluctuations in the window geometry and specify the mean window position by a theta function $\Theta(\pm x')$, where $x'(t) = [x - x_0(t)] \cos \theta(t) + [y - y_0(t)] \sin \theta(t)$ measures distance from the window, $\theta(t)$ is the initially smaller angle between the elongation axis and the beam direction, and $(x_0(t), y_0(t))$ is the position of the center of the window.

With the quantities introduced above, we can define the relative coordinate, $\mathbf{R}_\lambda = \mathbf{R}_\lambda^+ - \mathbf{R}_\lambda^-$, the reduced mass, $\mu_\lambda = M_\lambda^+ M_\lambda^- / (M_\lambda^+ + M_\lambda^-)$, and the relative linear momentum,

$$\begin{aligned} \mathbf{P}_\lambda &= \mu_\lambda \dot{\mathbf{R}}_\lambda = \frac{M_\lambda^- \mathbf{P}_\lambda^+ - M_\lambda^+ \mathbf{P}_\lambda^-}{M_\lambda^+ + M_\lambda^-} \\ &= \mu_\lambda [\dot{R}_\lambda \hat{\mathbf{e}}_R + R_\lambda \dot{\theta}_\lambda \hat{\mathbf{e}}_\theta]. \end{aligned} \quad (7)$$

Here, $\dot{\mathbf{R}}_\lambda = \dot{\mathbf{R}}_\lambda^+ - \dot{\mathbf{R}}_\lambda^-$ denotes the relative velocity vector, where the velocities of the projectile- and target-like fragments can be defined by $\dot{\mathbf{R}}_\lambda^\pm = \dot{\mathbf{P}}_\lambda^\pm / M_\lambda^\pm$. In the second line

of Eq. (7), the relative velocity is decomposed into the radial and tangential components with the unit vectors in respective directions,

$$\hat{\mathbf{e}}_R = \cos \theta \hat{\mathbf{e}}_x + \sin \theta \hat{\mathbf{e}}_y, \quad (8)$$

$$\hat{\mathbf{e}}_\theta = -\sin \theta \hat{\mathbf{e}}_x + \cos \theta \hat{\mathbf{e}}_y. \quad (9)$$

Neglecting the rate of change of the reduced mass, one finds the following expression for the rate of change of the relative momentum:

$$\begin{aligned} \frac{d\mathbf{P}_\lambda}{dt} &= \mu_\lambda [(\ddot{R}_\lambda - R_\lambda \dot{\theta}_\lambda^2) \hat{\mathbf{e}}_R + (R_\lambda \ddot{\theta}_\lambda + 2\dot{R}_\lambda \dot{\theta}_\lambda) \hat{\mathbf{e}}_\theta] \\ &= \left(\frac{dK_\lambda}{dt} - \frac{L_\lambda^2}{\mu_\lambda R_\lambda^3} \right) \hat{\mathbf{e}}_R + \left(\frac{1}{R_\lambda} \frac{dL_\lambda}{dt} \right) \hat{\mathbf{e}}_\theta, \end{aligned} \quad (10)$$

where we have introduced the radial component of the relative linear momentum K_λ and the relative orbital angular momentum L_λ defined as

$$K_\lambda \equiv \hat{\mathbf{e}}_R \cdot \mathbf{P}_\lambda, \quad (11)$$

$$L_\lambda \equiv \mu_\lambda R_\lambda^2 \dot{\theta}. \quad (12)$$

The first and the second terms of Eq. (10) denote the rate of changes of the radial and the tangential components, respectively.

C. Stochastic equations for the relative momenta

In the SMF approach, we can express the rate of change of the projectile- and target-like fragments in an event λ as

$$\frac{d\mathbf{P}_\lambda^\pm}{dt} = \pm m \int d\mathbf{r} \delta(x') \dot{x}' \mathbf{j}_\lambda(\mathbf{r}, t) + m \int d\mathbf{r} \Theta(\pm x') \frac{\partial \mathbf{j}_\lambda(\mathbf{r}, t)}{\partial t}. \quad (13)$$

Employing the TDHF equation for the single-particle orbitals in the event λ , it is possible to write down the rate of change of the radial and the tangential components of the linear momentum of the fragments in the following form:

$$\begin{aligned} \hat{\mathbf{e}}_\alpha \cdot \frac{d\mathbf{P}_\lambda^\pm}{dt} &= \pm \int d\mathbf{r} \delta(x') \dot{x}' m \hat{\mathbf{e}}_\alpha \cdot \mathbf{j}_\lambda(\mathbf{r}, t) \\ &\quad - \int d\mathbf{r} \Theta(\pm x') \nabla \cdot \sum_{ij} \left(\mathbf{A}_{ji}^\alpha - \mathbf{B}_{ji}^\alpha \right) \rho_{ji}^\lambda \\ &\quad + [\text{Potential terms}] \end{aligned} \quad (14)$$

with

$$\mathbf{A}_{ji}^\alpha = \frac{\hbar^2}{4m} \left[\phi_i(\mathbf{r}, t; \lambda) \nabla (\hat{\mathbf{e}}_\alpha \cdot \nabla \phi_j^*(\mathbf{r}, t; \lambda)) + \text{c.c.} \right], \quad (15)$$

$$\mathbf{B}_{ji}^\alpha = \frac{\hbar^2}{4m} \left[(\nabla \phi_i(\mathbf{r}, t; \lambda)) \hat{\mathbf{e}}_\alpha \cdot \nabla \phi_j^*(\mathbf{r}, t; \lambda) + \text{c.c.} \right], \quad (16)$$

where $\hat{\mathbf{e}}_\alpha$ indicates the unit vector in the radial ($\alpha = R$) or the tangential ($\alpha = \theta$) direction. The '[Potential terms]' in Eq. (14) represents terms associated with mean-field potentials other than the kinetic term in the single-particle Hamiltonian in the event λ .

From Eq. (14), we can derive a Langevin equation for the rate of change of the relative linear momentum,

$$\frac{d\mathbf{P}_\lambda}{dt} = \int d\mathbf{r} g(x') \dot{x}' m \mathbf{j}_\lambda(\mathbf{r}, t) + [\text{Potential terms}] + \mathbf{f}^\lambda(t), \quad (17)$$

where the first and the second terms represent the forces arising from the motion of the window plane and the potential terms, respectively. The quantity $\mathbf{f}^\lambda(t)$ is the fluctuating dynamical force due to nucleon exchange between projectile- and target-like fragments. Its radial ($\alpha = R$) and tangential ($\alpha = \theta$) components are given by

$$f_\alpha^\lambda(t) = \sum_{ij} Y_{ji}^\alpha(t) \rho_{ji}^\lambda, \quad (18)$$

where we have introduced a shorthand notation,

$$Y_{ji}^\alpha(t) \equiv \int d\mathbf{r} g(x') \hat{e}_R \cdot (\mathbf{A}_{ji}^\alpha(t) - \mathbf{B}_{ji}^\alpha(t)). \quad (19)$$

In obtaining this result we employed a partial integration in Eq. (14) and used the following relations:

$$\frac{\partial}{\partial x} \Theta(x') = \delta(x') \cos \theta, \quad (20)$$

$$\frac{\partial}{\partial y} \Theta(x') = \delta(x') \sin \theta. \quad (21)$$

In Eq. (17) the delta function has been replaced with a smoothing function $\delta(x') \rightarrow g(x')$ expressed as a Gaussian,

$$g(x') = \frac{1}{\sqrt{2\pi\kappa}} \exp\left[-\frac{1}{2} \left(\frac{x'}{\kappa}\right)^2\right], \quad (22)$$

with a dispersion $\kappa = 1.0$ fm which is on the same order as the lattice spacing in the numerical calculations. By projecting Eq. (17) along the radial and the tangential directions, together with Eq. (10), we obtain two coupled Langevin equations for the radial and angular momenta [41, 42]:

$$\frac{dK_\lambda}{dt} - \frac{L_\lambda^2}{\mu_\lambda R_\lambda^3} = \int d\mathbf{r} g(x') \dot{x}' m \hat{e}_R \cdot \mathbf{j}_\lambda(\mathbf{r}, t) + f_R^\lambda(t) + [\text{Potential terms}], \quad (23)$$

$$\frac{1}{R_\lambda} \frac{dL_\lambda}{dt} = \int d\mathbf{r} g(x') \dot{x}' m \hat{e}_\theta \cdot \mathbf{j}_\lambda(\mathbf{r}, t) + f_\theta^\lambda(t) + [\text{Potential terms}]. \quad (24)$$

In the right-hand side of these expressions, the first and the third terms represent the force due to the motion of the window plane and the conservative force due to nuclear and electrical potential energies, respectively. The fluctuating forces, $f_R^\lambda(t)$ and $f_\theta^\lambda(t)$, represent the dynamical forces arising from nucleon exchange between projectile- and target-like fragments. These dynamical forces provide the dominant mechanism for the dissipation and fluctuations of the relative momentum in damped collisions of heavy ions, such as deep-inelastic and quasifission processes.

The ensemble average of these equations of motion are equivalent to the TDHF description for the radial and angular

components of the relative linear momentum. Consequently, we use the mean values of TKE and the orbital angular momentum obtained from the TDHF approach. We employ the Langevin equations, Eqs. (23) and (24), for describing fluctuations around their mean values. There are two different sources for fluctuations of the dynamical forces $f_R^\lambda(t)$ and $f_\theta^\lambda(t)$ induced by nucleon exchange: (i) fluctuations due to different set of wave functions in each event λ , and (ii) fluctuations introduced by the stochastic part $\delta\rho_{ji}^\lambda$ of the density matrix at the initial state. The former part of fluctuations can be approximately described in terms of the fluctuating components of the radial and angular momentum as $f_R^\lambda(t) \rightarrow f_R^{\text{diss}}(K_\lambda)$ and $f_\theta^\lambda(t) \rightarrow f_\theta^{\text{diss}}(L_\lambda)$. Here, $f_R^{\text{diss}}(K_\lambda)$ and $f_\theta^{\text{diss}}(L_\lambda)$ are the mean values of the radial and tangential components of the dissipative part of the dynamical forces expressed in terms of fluctuating radial and angular momenta, respectively. We assume that the amplitude of the fluctuations are sufficiently small, so that we can linearize the Langevin equations, Eq. (23) and (24), around the mean values to give

$$\frac{\partial}{\partial t} \delta K_\lambda - \frac{2L_\lambda}{\mu R^3} \delta L_\lambda = \left(\frac{\partial f_R^{\text{diss}}}{\partial K} \right) \delta K_\lambda + \delta f_R^\lambda, \quad (25)$$

$$\frac{\partial}{\partial t} \delta L_\lambda = \left(\frac{\partial f_\theta^{\text{diss}}}{\partial L} \right) \delta L_\lambda + R \delta f_\theta^\lambda, \quad (26)$$

where $\delta K_\lambda = K_\lambda - \overline{K_\lambda}$ and $\delta L_\lambda = L_\lambda - \overline{L_\lambda}$ are the fluctuating components of the radial and angular momenta, respectively. The fluctuating forces originating from the potential energy terms are expected to have a small effect on the fluctuations of the relative momentum. In these expressions, we neglect these forces as well as the force due to the motion of the window given by the first terms in the right-hand side of Eqs. (23) and (24). Also, we neglect the fluctuations in the reduced mass and the relative distance between the centers of the fragments. The quantities, $\mu(t)$, $R(t)$, and $L(t)$, are, respectively, the mean values of the reduced mass, the relative distance, and the relative orbital angular momentum of the colliding system, which are determined by the TDHF equation. The derivatives of dissipative forces on the right-hand side of Eqs. (25) and (26) are related to the reduced radial and tangential friction coefficients:

$$\frac{\partial f_R^{\text{diss}}}{\partial K} = -\gamma_R(t), \quad (27)$$

$$\frac{\partial f_\theta^{\text{diss}}}{\partial L} = -\gamma_\theta(t). \quad (28)$$

An analysis of the radial friction force and the reduced friction coefficients are presented in Appendix B.

Multiplying both sides of Eqs. (25) and (26) by δK_λ and δL_λ , respectively, and taking the ensemble average, we obtain a set of coupled differential equations for the variances [43–

45],

$$\frac{d\sigma_{KK}^2}{dt} - \frac{4L}{\mu R^3} \sigma_{KL}^2 = -2\gamma_R \sigma_{KK}^2 + 2D_{KK}, \quad (29)$$

$$\frac{d\sigma_{LL}^2}{dt} = -2\gamma_\theta \sigma_{LL}^2 + 2R^2 D_{LL}, \quad (30)$$

$$\frac{d\sigma_{KL}^2}{dt} - \frac{2L}{\mu R^3} \sigma_{LL}^2 = -2(\gamma_R + \gamma_\theta) \sigma_{KL}^2 + R(D_{KL} + D_{LK}), \quad (31)$$

where the variances are defined as $\sigma_{KK}^2(t) = \overline{\delta K_\lambda(t) \delta K_\lambda(t)}$, $\sigma_{LL}^2(t) = \overline{\delta L_\lambda(t) \delta L_\lambda(t)}$, and $\sigma_{KL}^2(t) = \overline{\delta K_\lambda(t) \delta L_\lambda(t)}$. Here, $D_{\alpha\beta}(t)$ denotes the momentum diffusion coefficients ($\alpha, \beta = K, L$)¹, which are expressed on a microscopic basis in terms of single-particle orbitals within the TDHF approach.

III. TOTAL KINETIC ENERGY DISTRIBUTION WITHIN THE SMF APPROACH

A. Momentum diffusion coefficients

The momentum diffusion coefficients for the radial and angular momenta are defined as the time integral over the history of the autocorrelation functions of the stochastic forces,

$$D_{\alpha\beta}(t) = \int_0^t dt' \overline{\delta f_\alpha^\lambda(t) \delta f_\beta^\lambda(t')}. \quad (32)$$

The stochastic parts of the radial and tangential forces are given by,

$$\delta f_\alpha^\lambda(t) = \sum_{ij} Y_{ji}^\alpha(t) \delta \rho_{ji}^\lambda. \quad (33)$$

Using the basic postulate of the SMF approach, we can analytically take the ensemble average, and the correlation functions of the random force on radial and tangential directions read

$$\overline{\delta f_\alpha^\lambda(t) \delta f_\beta^\lambda(t')} = \text{Re} \left[\sum_{p \in \text{P}, h \in \text{T}} Y_{hp}^\alpha(t) Y_{hp}^{\beta*}(t') + \sum_{p \in \text{T}, h \in \text{P}} Y_{hp}^\alpha(t) Y_{hp}^{\beta*}(t') \right]. \quad (34)$$

In this expression, the summations in the first term run over the particle states originating from the projectile $p \in \text{P}$ and the hole states originating from the target $h \in \text{T}$, while in the second term the summations run in the opposite way. By adding and subtracting the hole-hole terms, the first term in this expression can be written as,

$$\sum_{p \in \text{P}, h \in \text{T}} Y_{hp}^\alpha(t) Y_{hp}^{\beta*}(t') = \sum_{h \in \text{T}, a \in \text{P}} Y_{ha}^\alpha(t) Y_{ha}^{\beta*}(t') - \sum_{h \in \text{T}, h' \in \text{P}} Y_{hh'}^\alpha(t) Y_{hh'}^{\beta*}(t'). \quad (35)$$

In the first term, the summation $a \in \text{P}$ runs over the complete set of states originating from the projectile. We introduce a similar subtraction in the second term of Eq. (34). As shown in Appendix A, using the closure relation in a diabatic approximation of the TDHF orbitals, it is possible to eliminate the complete set of the projectile (target) states in the first (second) term. As a result, the radial, the tangential and the mixed diffusion coefficients are given by the following compact expression:

$$D_{\alpha\beta}(t) = \int_0^t d\tau \int d\mathbf{r} \tilde{g}(x') \left[G_{\text{T}}(\tau) J_{\alpha\beta}^{\text{T}}(\mathbf{r}, \bar{t}) + G_{\text{P}}(\tau) J_{\alpha\beta}^{\text{P}}(\mathbf{r}, \bar{t}) \right] - \int_0^t d\tau \text{Re} \left[\sum_{h \in \text{T}, h' \in \text{P}} Y_{hh'}^\alpha(t) Y_{hh'}^{\beta*}(t - \tau) + \sum_{h \in \text{P}, h' \in \text{T}} Y_{hh'}^\alpha(t) Y_{hh'}^{\beta*}(t - \tau) \right]. \quad (36)$$

In the first line, the quantity $J_{\alpha\beta}^{\text{T}}(\mathbf{r}, \bar{t})$ is given by

$$J_{\alpha\beta}^{\text{T}}(\mathbf{r}, \bar{t}) = \frac{\hbar}{m} \sum_{h \in \text{T}} [m u_\alpha^h(\mathbf{r}, \bar{t})] [m u_\beta^h(\mathbf{r}, \bar{t})] \times \left| \text{Im} [\phi_h^*(\mathbf{r}, \bar{t}) \hat{e}_R \cdot \nabla \phi_h(\mathbf{r}, \bar{t})] \right|, \quad (37)$$

where $\bar{t} = (t+t')/2 = t - \tau/2$. This expression represents the magnitude of the nucleon flux that carries the product of the momentum components $m u_\alpha^h(\mathbf{r}, \bar{t})$ and $m u_\beta^h(\mathbf{r}, \bar{t})$ from the target-like fragment in the perpendicular ($\alpha, \beta = R$) and tangential ($\alpha, \beta = \theta$) directions to the window plane. The quantity $J_{\alpha\beta}^{\text{P}}(\mathbf{r}, t - \tau/2)$ is given by a similar expression and it represents the magnitude of the nucleon flux from the projectile-like fragment. The radial and tangential components of the nucleon flow velocities are determined by

$$u_\alpha^h(\mathbf{r}, \bar{t}) = \frac{\hbar}{m} \frac{\text{Im} [\phi_h^{\alpha*}(\mathbf{r}, \bar{t}) \hat{e}_\alpha \cdot \nabla \phi_h^\alpha(\mathbf{r}, \bar{t})]}{|\phi_h(\mathbf{r}, \bar{t})|^2}. \quad (38)$$

We observe that there is a close analogy between the quantal expression of the diffusion coefficients and the classical ones in a random walk problem. The first term in the quantal expression (36) gives the sum of the nucleon flux across the window from the target-like to the projectile-like fragments and vice versa, which is integrated over the memory. Each nucleon transfer across the window in both directions carries the product of the momentum components which increases the rate of change of the momentum dispersion. This is analogous to the random walk problem, in which the diffusion coefficient is given by the sum of the rate for forward and backward steps. The second term in the quantal expression (36) stands for the Pauli blocking effects in the nucleon transfer mechanism, which does not have a classical counterpart. The quantities in the Pauli blocking factors are determined by hole-hole elements of the matrices $Y_{hh'}^\alpha(t)$ and $Y_{hh'}^{\beta*}(t)$ which are defined in Eq. (19) with Eqs. (15) and (16).

¹ Note that we use the same notation (α, β) to indicate the radial and tangential directions (R, θ) and the radial and angular momenta (K, L).

B. Total kinetic energy distribution

It is possible to determine the joint probability distribution function of the radial linear momentum K and the orbital angular momentum L for each initial orbital angular momentum l , $P_l(K, L)$, employing the coupled Langevin equations, Eqs. (25) and (26). It is well known that these coupled Langevin equations are equivalent to the Fokker-Planck description for the joint probability distribution $P_l(K, L)$ [46]. When the radial and tangential friction forces have linear dependence on the radial and the angular momenta, the solution of the joint probability distribution can be expressed as a correlated Gaussian function:

$$P_l(K, L) = \frac{\exp[-C_l(K, L)]}{2\pi\sigma_{KK}(l)\sigma_{LL}(l)\sqrt{1-\eta_l^2}}, \quad (39)$$

where

$$C_l(K, L) = \frac{1}{2(1-\eta_l^2)} \left[\left(\frac{K - K_l}{\sigma_{KK}(l)} \right)^2 + \left(\frac{L - L_l}{\sigma_{LL}(l)} \right)^2 - 2\eta_l \left(\frac{K - K_l}{\sigma_{KK}(l)} \right) \left(\frac{L - L_l}{\sigma_{LL}(l)} \right) \right]. \quad (40)$$

Here, the correlation factor is defined as $\eta_l \equiv \sigma_{KL}^2(l)/\sigma_{KK}(l)\sigma_{LL}(l)$. $K_l \equiv \bar{K}_\lambda(l)$ and $L_l \equiv \bar{L}_\lambda(l)$ denote the mean values of the radial and the angular momenta for each value of the initial orbital angular momentum l , respectively, which are determined by solving the TDHF equation.

The mean values of the radial and angular momenta, K_l and L_l , are obtained by solving the TDHF equation. In practice, we follow the reaction dynamics up to a certain instant, say $t = t_f$, at which binary products are well separated spatially. Denoting the relative distance at this instant as $R_f = R(t_f)$, the asymptotic value of TKE of the outgoing fragments is given by $E_{\text{kin}}^\infty(K, L) = K^2/2\mu + L^2/2\mu R_f^2 + Z_1 Z_2 e^2/R_f$. For a given initial angular momentum l , we define the TKE distribution $G_l(E)$ as

$$G_l(E) = \int dK dL \delta(E - E_{\text{kin}}^\infty(K, L)) P_l(K, L). \quad (41)$$

Note that K and L in the above expression correspond to the radial and the angular momenta at the instant $t = t_f$, respectively, and E stands here for the asymptotic TKE. It is to mention that μ and $Z_{1,2}$ are, in general, l dependent quantities, and the fluctuations in the mass and charge asymmetries may affect the TKE fluctuations. However, we neglect the effects of mass and charge fluctuations on the TKE distribution and retain the mean values of the mass and charge asymmetry for each angular momentum.

In practice, the mixed diffusion coefficients, $D_{KL}(t)$ and $D_{LK}(t)$, are expected to be much smaller than the radial and the angular momentum diffusion coefficients, $D_{KK}(t)$ and $D_{LL}(t)$. Hence, in the present work, we neglect the mixed dispersion term $\sigma_{KL}(t)$ in Eq. (29) and the coupling between the radial and angular momenta. In such a case, the expression can be greatly simplified by taking the asymptotic limit,

$R \rightarrow \infty$, leading to

$$G_l(E) = \int dK^\infty \delta(E - E_{\text{kin}}^\infty(K^\infty)) P_l(K^\infty), \quad (42)$$

where $E_{\text{kin}}^\infty(K) = K^2/2\mu$ and $P_l(K)$ is the probability distribution of the radial momentum. Notice that by taking the limit $R \rightarrow \infty$ the centrifugal part of the kinetic energy and the Coulomb energy entirely transformed into the radial TKE, and K^∞ in Eq. (42) corresponds to the asymptotic value of the radial momentum for $R \rightarrow \infty$. After taking the integral over the angular momentum variable, the asymptotic radial momentum distribution becomes a simple Gaussian,

$$P_l(K) = \frac{1}{\sqrt{2\pi}\sigma_{KK}(l)} \exp\left[-\frac{1}{2}\left(\frac{K - K_l^\infty}{\sigma_{KK}(l)}\right)^2\right], \quad (43)$$

where the mean value of the asymptotic radial momentum is related to the mean asymptotic TKE from TDHF, $E_{\text{kin}}^\infty(l)$, by $K_l^\infty = (2\mu E_{\text{kin}}^\infty(l))^{1/2}$. After a trivial integration, we obtain the asymptotic TKE distribution,

$$G_l(E) = \frac{1}{\sqrt{8\pi E} \tilde{\sigma}_{KK}(l)} \exp\left[-\frac{1}{2}\left(\frac{\sqrt{E} - \sqrt{E_{\text{kin}}^\infty(l)}}{\tilde{\sigma}_{KK}(l)}\right)^2\right], \quad (44)$$

where $\tilde{\sigma}_{KK}(l) \equiv \sigma_{KK}(l)/\sqrt{2\mu}$. To obtain the radial dispersion $\sigma_{KK}(t)$, we solve the quantal diffusion equation for the radial component,

$$\frac{d\sigma_{KK}^2}{dt} = -2\gamma_R \sigma_{KK}^2 + 2D_{KK}. \quad (45)$$

We note that the unit of the TKE distribution G_l is MeV^{-1} , hence the fraction of events with final TKE in the energy range ΔE in MeV is given by $G_l \Delta E$.

IV. RESULTS FOR XE+PB COLLISIONS

In this section, as the first application of the proposed formalism given in the preceding sections, we present calculations of the TKE distribution for the $^{136}\text{Xe}+^{208}\text{Pb}$ reaction at $E_{\text{c.m.}} = 526$ MeV, for which extensive experimental data reported by Kozulin *et al.* [33] are available. TDHF calculations were carried out for a range of initial orbital angular momenta l . The results of TDHF calculations for a set of observables in the $^{136}\text{Xe}+^{208}\text{Pb}$ reaction at $E_{\text{c.m.}} = 526$ MeV are presented in Table I. We mention here that for the $^{136}\text{Xe}+^{208}\text{Pb}$ system the average numbers of transferred nucleons are small, reflecting a small charge asymmetry and possible shell effects in the reactants. Nucleons are, however, actively exchanged during the collision, which is the source of dissipation and fluctuations of observables, such as mass, charge, TKE, and scattering angles, in low-energy heavy-ion reactions. For this reaction, mean TKEL reaches around 175 MeV for small angular momenta, while contact time is rather short ($\lesssim 2$ zs). Because of the short contact time the composite system does not rotate much in the reaction plane. We note that fragments are

TABLE I. A list of numerical results of the TDHF calculations for the $^{136}\text{Xe}+^{208}\text{Pb}$ reaction at $E_{c.m.} = 526\text{ MeV}$. From left to right columns, it shows: the initial orbital angular momentum, l , in \hbar , the final average relative orbital angular momentum, L_f , in \hbar , neutron and proton numbers of projectile-like (target-like) fragment, N_1 and Z_1 (N_2 and Z_2), mean total kinetic energy loss (TKEL) in MeV, contact time, t_{contact} , in fm/c, scattering angles in center-of-mass frame, $\theta_{c.m.}$, and those in laboratory frame for projectile-like (target-like) fragment, ϑ_1^{lab} (ϑ_2^{lab}), in degrees. The contact time is defined as duration in which the minimum density between two colliding nuclei exceeds half the saturation density, $\rho_{\text{sat}}/2 = 0.08\text{ fm}^{-3}$.

l (\hbar)	L_f (\hbar)	N_1	Z_1	N_2	Z_2	TKEL (MeV)	t_{contact} (fm/c)	$\theta_{c.m.}$ (deg)	ϑ_1^{lab} (deg)	ϑ_2^{lab} (deg)
0	0	82.3	55.1	125.0	80.9	173.1	661.4	180.0	180.0	0.0
50	39	82.4	55.1	124.9	80.8	177.0	646.0	150.1	96.4	13.5
100	78	82.0	54.5	125.4	81.5	175.6	611.8	123.1	72.9	25.4
110	85	81.9	54.3	125.5	81.6	175.1	593.2	118.2	69.5	27.5
120	95	81.8	54.3	125.6	81.7	175.0	591.4	113.3	66.2	29.6
130	104	81.7	54.3	125.7	81.7	175.3	586.6	108.6	63.0	31.6
140	114	81.9	54.4	125.5	81.5	175.0	571.0	104.0	60.0	33.6
150	124	82.4	54.7	125.0	81.2	174.3	555.2	99.7	57.1	35.6
160	134	83.1	55.2	124.3	80.7	171.9	538.6	95.9	54.6	37.4
170	142	83.7	55.6	123.7	80.3	169.4	529.4	92.5	52.5	39.0
180	149	83.9	55.8	123.5	80.2	168.5	517.6	89.7	50.7	40.3
190	158	83.6	55.6	123.9	80.3	167.4	474.0	87.1	49.3	41.3
200	166	83.0	55.4	124.5	80.6	166.0	462.4	85.2	48.4	42.0
210	173	82.7	55.2	124.9	80.7	161.0	440.2	84.1	47.9	42.6
220	179	82.3	55.0	125.3	80.9	154.9	409.4	83.3	47.8	43.1
230	185	81.8	54.8	125.8	81.2	149.1	378.4	82.5	47.6	43.5
240	194	81.5	54.6	126.2	81.3	140.7	343.6	81.7	47.4	44.1
250	203	81.3	54.5	126.4	81.5	129.8	303.2	81.0	47.4	44.8
260	214	81.2	54.4	126.6	81.5	117.1	257.2	80.5	47.5	45.5
270	225	81.2	54.4	126.6	81.5	103.5	226.0	80.0	47.5	46.2
280	240	81.4	54.5	126.5	81.5	86.0	192.4	79.5	47.6	47.2
290	258	81.5	54.5	126.4	81.5	66.8	146.8	79.0	47.8	48.2
300	277	81.5	54.4	126.4	81.6	48.9	100.8	78.5	47.9	49.0
310	295	81.6	54.3	126.4	81.7	32.7	44.2	78.1	48.0	49.8
320	311	81.7	54.2	126.2	81.8	16.9	0.0	77.9	48.2	50.4
330	325	81.9	54.1	126.1	81.9	8.0	0.0	77.4	48.1	51.0
340	337	81.9	54.0	126.1	82.0	4.7	0.0	76.4	47.5	51.6
350	347	81.9	54.0	126.1	82.0	3.3	0.0	75.2	46.7	52.3

emitted outside the experimental angular coverage (25° – 70° in the laboratory frame) in events below $l < 100\hbar$ in TDHF calculations.

In order to evaluate the TKE distribution, we have further extended our three-dimensional parallel TDHF code, which was applied for various systems [17, 47–53] and was recently incorporated with the SMF approach [31]. For the computational details we refer readers to our recent article, Ref. [31]. To obtain the TKE distribution (44), we need to evaluate the asymptotic value of the radial momentum dispersion $\sigma_{KK}(l)$ for each value of the initial angular momentum l by solving Eq. (45). The radial momentum diffusion coefficient $D_{KK}(t)$

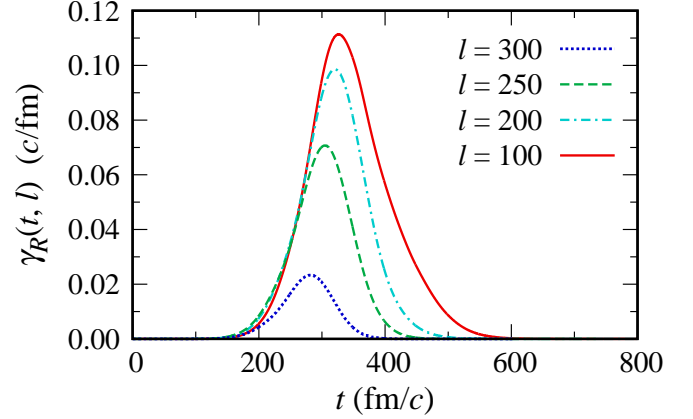


FIG. 2. Reduced radial friction coefficients γ_R in the $^{136}\text{Xe}+^{208}\text{Pb}$ reaction at $E_{c.m.} = 526\text{ MeV}$ with initial orbital angular momenta of $l = 100, 200, 250,$ and 300 (in units of \hbar) are shown as functions of time.

is directly computed from occupied single-particle orbitals within the TDHF approach with the quantal expression given in Eq. (36). On the other hand, it is not trivial how to determine the radial friction coefficient directory from TDHF. Nevertheless, using the analogy to the random walk problem, we have extracted from TDHF an approximate expression for the radial friction force and the radial friction coefficients. Details of this analysis are given in Appendix B.

In Figs. 2–4, we show examples of the computational results for the collisions of $^{136}\text{Xe}+^{208}\text{Pb}$ at $E_{c.m.} = 526\text{ MeV}$ for four typical initial angular momenta, l [$= 100$ (solid line), 200 (dash-dotted line), 250 (dashed line), and 300 (dotted line) in units of \hbar], as functions of time. Figure 2 shows the reduced radial friction coefficients $\gamma_R(t, l)$ given by Eq. (B9), which were extracted from TDHF employing the method explained in detail in Appendix B. We observe that the radial friction coefficient develops when two nuclei collide at around $t = 200$ – 400 fm/c . The magnitude of the friction coefficient increases with decreasing the initial orbital angular momentum l , for which contact times are longer, indicating that larger amount of the relative kinetic energy is converted into internal exci-

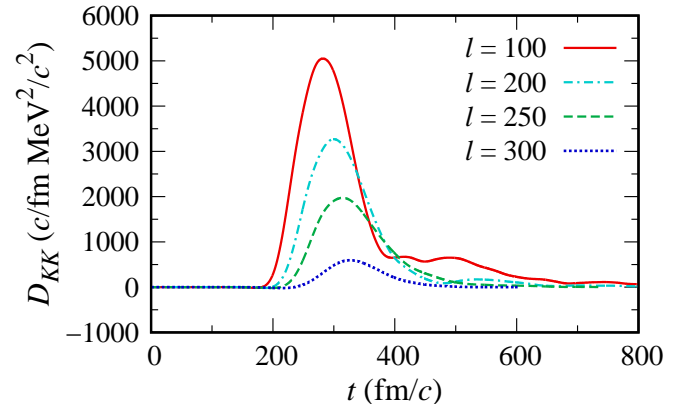


FIG. 3. Radial-momentum diffusion coefficients in the $^{136}\text{Xe}+^{208}\text{Pb}$ reaction at $E_{c.m.} = 526\text{ MeV}$ with initial orbital angular momenta of $l = 100, 200, 250,$ and 300 (in units of \hbar) are shown as functions of time.

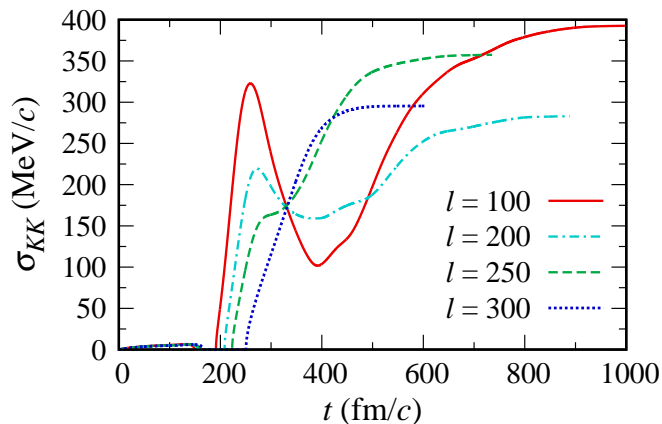


FIG. 4. Variances of the radial momentum in the $^{136}\text{Xe}+^{208}\text{Pb}$ reaction at $E_{c.m.} = 526$ MeV with initial orbital angular momenta of $l = 100, 200, 250,$ and 300 (in units of \hbar) are shown as functions of time.

tations at smaller orbital angular momenta, as expected. In Fig. 3, we show the quantal momentum diffusion coefficient $D_{KK}(t)$ given by Eq. (36), which is calculated microscopically based on occupied single-particle orbitals within the TDHF approach. Again, the magnitude of the diffusion coefficient increases with decreasing the initial orbital angular momentum l . From the results, we find that the diffusion coefficient has a relatively long tail as compared to the friction coefficient shown in Fig. 2. It is related to the fact that the quantal diffusion coefficient is governed by nucleon exchange which lasts even after the turning point through a neck structure of the dinuclear system (cf. contact times shown in Table I).

Having the radial friction and momentum diffusion coefficients, $\gamma_R(t)$ and $D_{KK}(t)$, at hand, we solve the differential equation (45) and the results are shown in Fig. 4. From the figure, we see that the variances of the radial momentum σ_{KK} show somewhat complicated behavior as a function of time. The variance grows in time and saturates when two nuclei reparate. We notice that the asymptotic value of σ_{KK} is largest for $l = 100\hbar$ and decreases with increasing l values from $100\hbar$ to $200\hbar$, then increases for $l = 250\hbar$, and then decreases again for $l = 300\hbar$. One can also find this behavior in Table II, in which the asymptotic values of the radial momentum and TKE dispersions for a range of initial angular momenta are presented. We consider that in the present analysis the radial momentum dispersion is overpredicted for relatively large initial orbital angular momentum region ($l = (200\text{--}300)\hbar$), which are probably due to the approximate treatments of the radial friction coefficient. Since the primary purpose of the present work is to put the first step toward the microscopic description of the TKE distribution, developing a formalism based on the SMF approach, we leave further improvements of the description as future works.

Employing the expression of Eq. (44) we can obtain the TKE distribution and the results are shown in Fig. 5. Figure 5 illustrates the TKE distribution for the range of initial angular momenta $l = (100\text{--}350)\hbar$ in the l -TKE plane. We note that with the TKE distribution, G_l , we can evaluate the mean value

TABLE II. A list of numerical results of the SMF calculations for the $^{136}\text{Xe}+^{208}\text{Pb}$ reaction at $E_{c.m.} = 526$ MeV for a range of initial orbital angular momenta l . From left to right columns, it shows the asymptotic values of: the radial momentum dispersion, σ_{KK} , in MeV/c, the modified radial momentum dispersion, $\tilde{\sigma}_{KK} = \sigma_{KK}/\sqrt{2\mu}$, in $\text{MeV}^{1/2}$, and the dispersion of total kinetic energy (TKE), $\sigma_{\text{TKE}} \approx 2\tilde{\sigma}_{KK}\sqrt{E_{\text{kin}}^\infty}$, in MeV.

l (\hbar)	σ_{KK} (MeV/c)	$\tilde{\sigma}_{KK}$ ($\text{MeV}^{1/2}$)	σ_{TKE} (MeV)
0	553.7	1.406	52.84
50	497.2	1.263	47.18
100	392.7	0.999	37.38
110	367.3	0.934	35.01
120	342.4	0.871	32.64
130	319.4	0.813	30.44
140	298.3	0.759	28.43
150	277.9	0.706	26.48
160	268.7	0.681	25.65
170	266.0	0.674	25.45
180	261.0	0.661	25.00
190	265.4	0.672	25.47
200	282.9	0.718	27.23
210	302.8	0.769	29.37
220	317.0	0.805	31.03
230	329.7	0.838	32.55
240	344.2	0.876	34.38
250	357.5	0.910	36.22
260	366.6	0.933	37.75
270	365.5	0.930	38.25
280	352.0	0.896	37.58
290	330.3	0.840	36.02
300	295.4	0.752	32.84
310	233.6	0.595	26.41
320	152.0	0.387	17.46
330	85.8	0.218	9.94
340	34.5	0.088	4.01
350	36.2	0.092	4.21

of TKE as

$$\begin{aligned} \overline{\text{TKE}}(l) &= \int dE E G_l(E) \\ &\approx E_{\text{kin}}^\infty(l) + \tilde{\sigma}_{KK}^2(l). \end{aligned} \quad (46)$$

From Table II, we see that the asymptotic value of the largest dispersion occurs for $l = 0$. In this case, we find $\tilde{\sigma}_{KK}^2 = \sigma_{KK}^2/2\mu \approx 1.98$ MeV, which is much smaller than $E_{\text{kin}}^\infty(l) \approx 353$ MeV, confirming the correspondence with the mean TKE from TDHF. We can also calculate the variance of TKE for each value of angular momentum as

$$\begin{aligned} \sigma_{\text{TKE}}^2(l) &= \int dE (E - E_{\text{kin}}^\infty(l))^2 G_l(E) \\ &\approx 4\tilde{\sigma}_{KK}^2(l) E_{\text{kin}}^\infty(l). \end{aligned} \quad (47)$$

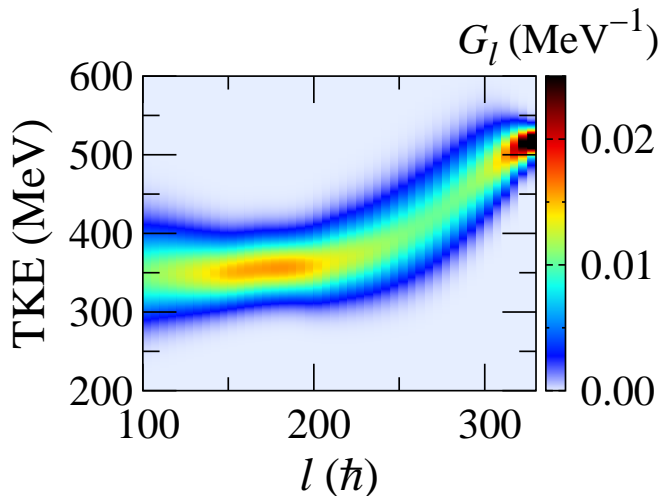


FIG. 5. The total kinetic energy (TKE) distribution, G_l defined by Eq. (44), is shown in the l -TKE plane, where l represents the initial orbital angular momentum of the reaction, calculated for the $^{136}\text{Xe}+^{208}\text{Pb}$ reaction at $E_{c.m.} = 526$ MeV.

Dispersion of TKE grows linearly with the square root of the mean value, $\sigma_{\text{TKE}} \approx 2\tilde{\sigma}_{KK}\sqrt{E_{\text{kin}}^\infty}$. For example for the initial angular momentum $l = 0$, dispersion is as large as $\sigma_{\text{TKE}} \approx 53$ MeV. This indicates the total excitation energy of the primary fragments have quite large dispersion values. Large values of dispersions of the excitation energies may have an important effect on deexcitation processes of the primary fragments.

Finally, to make a comparison with the experimental data [33], we evaluate the yield of the reaction outcomes as a function of total kinetic energy loss (TKEL, i.e., $E_{c.m.} - E_{\text{kin}}^\infty$) by summing up contributions from each initial orbital angular momentum,

$$Y(E_{c.m.} - E_{\text{kin}}^\infty) = Y_0 \sum_{l=100}^{350} (2l+1)G_l(E_{\text{kin}}^\infty). \quad (48)$$

The normalization constant Y_0 is adjusted to the data at a suitable point. The experimental setup in the work of Kozulin *et al.* [33] has an energy resolution of 25 MeV. To compare with the data, this experimental uncertainty should be accounted for by, e.g., a folding procedure of the calculated kinetic energy distribution. The folding procedure will introduce approximately a uniform shift in the kinetic energy distribution. Therefore, we consider that it does not change the shape of the calculated curve and the folding effect is absorbed by the normalization constant Y_0 .

Figure 6 shows a comparison of the calculations with experimental data for the collisions of $^{136}\text{Xe}+^{208}\text{Pb}$ at $E_{c.m.} = 526$ MeV. The measured TKEL distribution for two-body events (without sequential fission events) is shown by crosses with error bars. Open circles with error bars represent the experimental data from which the quasielastic component (a Gaussian fit to the data, shown by a dashed line) has been removed [33]. The calculated TKEL distribution according to Eq. (48) is shown by a solid line. From the figure we find that the calculations provide good description for strongly-damped

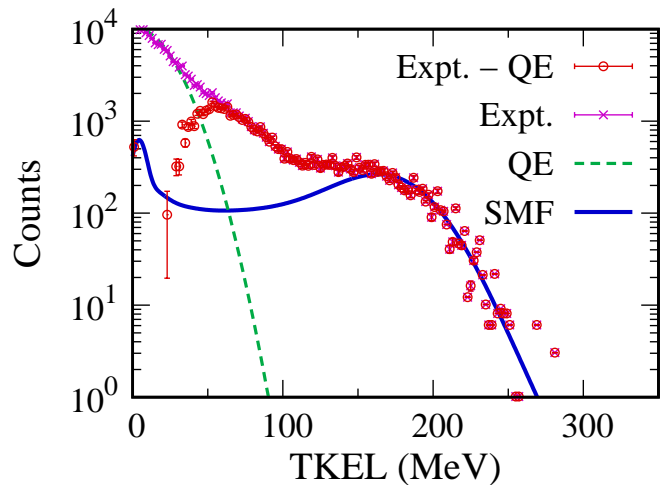


FIG. 6. The integrated total kinetic energy loss (TKEL) distribution for the $^{136}\text{Xe}+^{208}\text{Pb}$ reaction at $E_{c.m.} = 526$ MeV. Magenta crosses (open circles) with error bars represent the experimental data with (without) quasielastic contribution reported in Ref. [33]. A Gaussian fit of the quasielastic contribution is shown by the green dashed line. The results of SMF calculations are shown by the blue solid line, where the normalization constant is set to $Y_0 = 3.5$.

events with large energy losses, $\text{TKEL} \gtrsim 150$ MeV. However, it underestimates the count curve over the lower energy-loss segment. This behavior is a result of apparent large dispersions of the TKE distribution over the range $l = 200\hbar - 300\hbar$, which may be due to the over prediction of the radial momentum diffusion coefficients and/or the approximate description of the radial friction for the large angular momentum region. Although further improvements of the formalism are mandatory, we consider that the quantal diffusion approach based on the SMF theory provides a promising microscopic basis for quantifying kinetic energy dissipation and fluctuations in low-energy heavy-ion reactions.

V. SUMMARY

The stochastic mean-field (SMF) approach goes beyond the standard mean-field approximation, describing dynamical fluctuations of the collective motion in heavy-ion collisions at low energies. In the time-dependent Hartree-Fock (TDHF) approach, dynamical evolution of the colliding system is described by a single Slater determinant which is determined by a given set of initial conditions. In the SMF approach, on the other hand, an ensemble of the mean-field (TDHF) events for stochastically-generated initial conditions is considered. The initial conditions for each event are specified by the quantal and thermal fluctuations, and each event evolves according to the self-consistent mean-field Hamiltonian of that event. As a result, the SMF approach provides not only the mean values, but the entire distribution functions of the observables.

For low-energy heavy-ion reactions in which the colliding system maintains a dinuclear structure, instead of generating an ensemble of stochastic mean-field events, the evolution of the system can be described in terms of a few representative macroscopic variables, such as the relative linear momentum,

the orbital angular momentum, the mass and charge asymmetries of the colliding system. In such a case, we can deduce effective equations of motion for the macroscopic variables by adiabatic or geometric projection of the stochastically-generated mean-field events on a macroscopic subspace, in a manner similar to the Mori formalism [54]. For deep-inelastic or quasifission processes in which dinuclear structure is maintained, the geometric projection with the help of the window dynamics is more suitable to deduce the effective equations for the macroscopic variables. Being consistent with the Mori formalism, the effective equations for the macroscopic variables take the form of generalized Langevin equations which offer quantal diffusion description of the dynamical evolution of the colliding system. The Langevin equations are characterized by transport coefficients, i.e., diffusion and drift coefficients. It is possible to deduce analytical expressions for transport coefficients by carrying out suitable averages over the ensemble generated by the SMF approach. Employing the closure relation in the diabatic approximations of the TDHF wave functions, we can express the diffusion coefficients in terms of the occupied single-particle orbitals in TDHF. Therefore, it provides a very practical and powerful framework for the microscopic description of fluctuations of collective variables. This result is consistent with the quantal fluctuation-dissipation theorem of the non-equilibrium statistical mechanics [41, 42]. The theorem states that the diffusion coefficients which provide the source of fluctuations can be expressed in terms of the mean-field properties.

In previous studies we employed the quantal diffusion approach to investigate multinucleon transfer mechanism in low-energy heavy-ion collisions. In the present work, we have developed a formalism for describing the total kinetic energy (TKE) distributions of binary reaction products. We have deduced an effective transport equation for the relative linear momentum based on the SMF approach by the projection technique with the help of window dynamics. The radial and the tangential components of this equation provide quantal diffusion description of the radial linear momentum and the angular momentum of the relative motion, respectively.

As the first application of the present formalism, we have analyzed the total kinetic energy loss (TKEL) distribution for the $^{136}\text{Xe}+^{208}\text{Pb}$ reaction at $E_{c.m.} = 526$ MeV. For the analysis of the TKEL distribution, in addition to the radial momentum diffusion coefficient, it is necessary to determine the radial friction coefficient for different initial angular momenta. The one-body dissipation mechanism is contained in the mean-field description of the TDHF approach, but it is not trivial how to deduce the expression for the radial friction force and the radial friction coefficient from the TDHF description. We inferred an approximate expression for the radial friction force by using the analogy to the Langevin description of the random walk problem. We find that the dispersion of the TKE distribution reach rather large values which may have important effects in the deexcitation mechanism of the primary fragments. We have calculated the TKEL distribution by summing over the range of the initial angular momenta which is consistent with the experimental angular coverage. We have found that the calculations provide a reasonable description of the experimental data of the TKEL dis-

tribution for strongly-damped events with large energy losses (TKEL $\gtrsim 150$ MeV), but underestimate the data for lower values of TKEL (i.e., reactions at large initial orbital angular momenta). The underestimation of the TKEL distribution for large values of the orbital angular momentum may be partly due to the approximate description of the radial friction coefficient and/or the neglected coupling between the radial and tangential components of the linear momentum. This work put an important step forward for the microscopic description of low-energy heavy-ion reactions, including distributions of various observables, and further improvements of the proposed formalism are in order.

ACKNOWLEDGMENTS

The authors are grateful to Prof. E.M. Kozulin for providing us the experimental data. S.A. is very much thankful to F. Ayik for continuous support and encouragement. This work is supported in part by U.S. Department of Energy (DOE) Grant No. DE-SC0015513, and in part by JSPS Grant-in-Aid for Early-Career Scientists Grant No. 19K14704. This work used the computational resource of the HPCI system (Oakforest-PACS) provided by Joint Center for Advanced High Performance Computing (JCAHPC) through the HPCI System Project (Project ID: hp200022). This work also used (in part) computational resources of the Cray XC40 System at Yukawa Institute for Theoretical Physics (YITP), Kyoto University.

Appendix A: Momentum diffusion coefficient

In this Appendix, we derive the quantal expression of the momentum diffusion coefficient given by Eq. (36). Employing a partial integration in the expression $Y_{ha}^\alpha(t)$ in Eq. (19), we have

$$\begin{aligned}
 Y_{ha}^\alpha(t) &= \frac{\hbar^2}{m} \int d\mathbf{r}_1 \left[g(x'_1) [\hat{e}_\alpha \cdot \nabla_1 \hat{e}_R \cdot \nabla_1 \phi_h^*(\mathbf{r}_1, t)] \right. \\
 &\quad + \frac{1}{2} \hat{e}_\alpha \cdot \nabla_1 g(x'_1) \hat{e}_R \cdot \nabla_1 \phi_h^*(\mathbf{r}_1, t) \\
 &\quad + \frac{1}{2} \hat{e}_R \cdot \nabla_1 g(x'_1) \hat{e}_\alpha \cdot \nabla_1 \phi_h^*(\mathbf{r}_1, t) \\
 &\quad \left. + \frac{1}{4} [\hat{e}_\alpha \cdot \nabla_1 \hat{e}_R \cdot \nabla_1 g(x'_1)] \phi_h^*(\mathbf{r}_1, t) \right] \phi_a(\mathbf{r}_1, t),
 \end{aligned} \tag{A1}$$

and its complex conjugation,

$$\begin{aligned}
 Y_{ha}^{\alpha*}(t) &= \frac{\hbar^2}{m} \int d\mathbf{r}_1 \left[g(x'_1) [\hat{e}_\alpha \cdot \nabla_1 \hat{e}_R \cdot \nabla_1 \phi_h(\mathbf{r}_1, t)] \right. \\
 &\quad + \frac{1}{2} \hat{e}_\alpha \cdot \nabla_1 g(x'_1) \hat{e}_R \cdot \nabla_1 \phi_h(\mathbf{r}_1, t) \\
 &\quad + \frac{1}{2} \hat{e}_R \cdot \nabla_1 g(x'_1) \hat{e}_\alpha \cdot \nabla_1 \phi_h(\mathbf{r}_1, t) \\
 &\quad \left. + \frac{1}{4} [\hat{e}_\alpha \cdot \nabla_1 \hat{e}_R \cdot \nabla_1 g(x'_1)] \phi_h(\mathbf{r}_1, t) \right] \phi_a^*(\mathbf{r}_1, t).
 \end{aligned} \tag{A2}$$

With the diabatic property of the TDHF wave functions, we can shift the wave functions back and forth during short time intervals $\tau = t - t'$ to have an approximate relation,

$$\phi_a(\mathbf{r}, t') \approx \phi_a(\mathbf{r} - \mathbf{u}\tau, t), \quad (\text{A3})$$

where $\mathbf{u}\tau$ denotes a small displacement during the short time interval with flow velocity \mathbf{u} . Using the closure relation,

$$\sum_a \phi_a^*(\mathbf{r}_1, t) \phi_a(\mathbf{r}_2 - \mathbf{u}\tau, t) = \delta(\mathbf{r}_1 - \mathbf{r}_2 + \mathbf{u}\tau), \quad (\text{A4})$$

we obtain:

$$\sum_{h \in T, a \in P} Y_{ha}^\alpha(t) Y_{ha}^{\beta*}(t') = \sum_{h \in T} \iint d\mathbf{r}_1 d\mathbf{r}_2 \delta(\mathbf{r}_1 - \mathbf{r}_2 + \mathbf{u}_h\tau) \times W_h^\alpha(\mathbf{r}_1, t) W_h^{\beta*}(\mathbf{r}_2, t) \quad (\text{A5})$$

First, we consider the case for $\alpha = \beta = R$. The radial part $W_h^R(\mathbf{r}_1, t)$ reads

$$\begin{aligned} W_h^R(\mathbf{r}_1, t) = & \frac{\hbar^2}{m} \left[g(x'_1) [(\hat{\mathbf{e}}_R \cdot \nabla_1)(\hat{\mathbf{e}}_R \cdot \nabla_1) \phi_h(\mathbf{r}_1, t)] \right. \\ & + \frac{1}{2} \hat{\mathbf{e}}_R \cdot \nabla_1 g(x'_1) \hat{\mathbf{e}}_R \cdot \nabla_1 \phi_h(\mathbf{r}_1, t) \\ & + \frac{1}{2} \hat{\mathbf{e}}_R \cdot \nabla_1 g(x'_1) \hat{\mathbf{e}}_R \cdot \nabla_1 \phi_h(\mathbf{r}_1, t) \\ & \left. + \frac{1}{4} [(\hat{\mathbf{e}}_R \cdot \nabla_1)(\hat{\mathbf{e}}_R \cdot \nabla_1) g(x'_1)] \phi_h(\mathbf{r}_1, t) \right]. \end{aligned} \quad (\text{A6})$$

Using the expression for $g(x')$ given by Eq. (22), we find

$$\begin{aligned} W_h^K(\mathbf{r}_1, t) = & \frac{\hbar^2}{m} g(x'_1) \left[[(\hat{\mathbf{e}}_R \cdot \nabla_1)^2 \phi_h(\mathbf{r}_1, t)] \right. \\ & - \frac{x'_1}{\kappa^2} [\hat{\mathbf{e}}_R \cdot \nabla_1 \phi_h(\mathbf{r}_1, t)] \\ & \left. + \frac{1}{4\kappa^4} [x_1'^2 - \kappa^2] \phi_h(\mathbf{r}_1, t), \right] \end{aligned} \quad (\text{A7})$$

and its complex conjugation,

$$\begin{aligned} W_h^{K*}(\mathbf{r}_2, t) = & \frac{\hbar^2}{m} g(x'_2) \left[[(\hat{\mathbf{e}}_R \cdot \nabla_2)^2 \phi_h^*(\mathbf{r}_2, t)] \right. \\ & - \frac{x'_2}{\kappa^2} [\hat{\mathbf{e}}_R \cdot \nabla_2 \phi_h^*(\mathbf{r}_2, t)] \\ & \left. + \frac{1}{4\kappa^4} [x_2'^2 - \kappa^2] \phi_h^*(\mathbf{r}_2, t). \right] \end{aligned} \quad (\text{A8})$$

Let us introduce the following coordinate transformations,

$$\mathbf{R} = (\mathbf{r}_1 + \mathbf{r}_2)/2, \quad \mathbf{r} = \mathbf{r}_1 - \mathbf{r}_2, \quad (\text{A9})$$

and its inverse,

$$\mathbf{r}_1 = \mathbf{R} + \mathbf{r}/2, \quad \mathbf{r}_2 = \mathbf{R} - \mathbf{r}/2. \quad (\text{A10})$$

Because of the delta function, we can immediately carry out the integration over \mathbf{r} in Eq. (A5) and make the substitution for $\mathbf{r} = -\mathbf{u}_h\tau$, and introduce diabatic shifts in the wave functions,

$$\begin{aligned} \phi_h(\mathbf{r}_1, t) &= \phi_h(\mathbf{R} + \mathbf{r}/2, t) = \phi_h(\mathbf{R} - \mathbf{u}_h\tau/2, t) \\ &\approx \phi_h(\mathbf{R}, \bar{t}), \end{aligned} \quad (\text{A11})$$

$$\begin{aligned} \phi_h(\mathbf{r}_2, t) &= \phi_h(\mathbf{R} - \mathbf{r}/2, t) = \phi_h(\mathbf{R} + \mathbf{u}_h\tau/2, t) \\ &\approx \phi_h(\mathbf{R}, \bar{t}), \end{aligned} \quad (\text{A12})$$

with $\bar{t} \equiv (t + t')/2$. We can express product of the Gaussian factors as $g(x'_1)g(x'_2) = \tilde{g}(X')\tilde{G}(x')$, where

$$\tilde{g}(X') = \frac{1}{\sqrt{\pi\kappa}} \exp\left[-\left(\frac{X'}{\kappa}\right)^2\right], \quad (\text{A13})$$

$$\tilde{G}(X') = \frac{1}{\sqrt{4\pi\kappa}} \exp\left[-\left(\frac{X'}{2\kappa}\right)^2\right], \quad (\text{A14})$$

with $x' = \hat{\mathbf{e}}_R \cdot \mathbf{r} = -\hat{\mathbf{e}}_R \cdot \hat{\mathbf{u}}_h\tau = u_R^h\tau$ and $X' = \hat{\mathbf{e}}_R \cdot \mathbf{R}$, where $u_R^h(\mathbf{R}, \bar{t})$ denotes the component of the flow velocity of the hole states perpendicular to the window, which may, in general, depend on the mean position $\mathbf{R} = (\mathbf{r}_1 + \mathbf{r}_2)/2$ and the mean time $\bar{t} = (t + t')/2$. In the product $W_h^\alpha(\mathbf{r}_1, t)W_h^{\beta*}(\mathbf{r}_2, t')$, there are linear, second, third, and fourth order terms in x_1 and x_2 in the integrand of Eq. (A5). The integrand contains a product of two sharp Gaussians, $\tilde{g}(X')$ and $\tilde{G}(x')$, which provides the memory kernel in the integrand. Taking the averages over the memory kernel and over the sharp Gaussian $\tilde{g}(X')$, all terms in the integrand of Eq. (A5) which are proportional to the powers of x_1 and x_2 vanish. We obtain the similar results for other components of Eq. (A5) with $\alpha, \beta = R, \theta$, and we find

$$\begin{aligned} \sum_{h \in T, a \in P} Y_{ha}^\alpha(t) Y_{ha}^{\beta*}(t') = & \left(\frac{\hbar^2}{m}\right)^2 \sum_{h \in T} \int d\mathbf{R} \tilde{g}(X') \frac{G_T^h(\tau)}{|u_R^h(\mathbf{R}, \bar{t})|} \\ & \times [(\hat{\mathbf{e}}_\alpha \cdot \nabla)(\hat{\mathbf{e}}_R \cdot \nabla) \phi_h(\mathbf{R}, \bar{t})] \\ & \times [(\hat{\mathbf{e}}_\beta \cdot \nabla)(\hat{\mathbf{e}}_R \cdot \nabla) \phi_h(\mathbf{R}, \bar{t})]^*, \end{aligned} \quad (\text{A15})$$

where the memory kernel is defined as

$$G_T^h(\tau) = \frac{1}{\sqrt{4\pi}} \frac{1}{\tau_T^h} \exp\left[-\left(\frac{\tau}{2\tau_T^h}\right)^2\right], \quad (\text{A16})$$

with the memory time, $\tau_T^h = \kappa/|u_R^h|$. We can write the wave functions as $\phi_h(\mathbf{r}, t) = |\phi_h(\mathbf{r}, t)| \exp(iQ_h)$ [46]. Since the phase factor behaves like the velocity potential, neglecting derivative of the amplitude of the wave function, we have the approximate result:

$$\begin{aligned} (\hat{\mathbf{e}}_R \cdot \nabla) \phi_h &\approx i\phi_h \hat{\mathbf{e}}_R \cdot \nabla Q_h \\ &= i\phi_h(\mathbf{R}, \bar{t}) \frac{m}{\hbar} u_R^h(\mathbf{R}, \bar{t}). \end{aligned} \quad (\text{A17})$$

In a similar manner, we can express the second derivative of the wave function as,

$$\begin{aligned} (\hat{\mathbf{e}}_\theta \cdot \nabla)(\hat{\mathbf{e}}_R \cdot \nabla) \phi_h &\approx i[(\hat{\mathbf{e}}_\theta \cdot \nabla) \phi_h(\mathbf{R}, \bar{t})] u_R^h(\mathbf{R}, \bar{t}) \\ &\approx -\phi_h(\mathbf{R}, \bar{t}) \frac{m^2}{\hbar^2} u_\theta^h(\mathbf{R}, \bar{t}) u_R^h(\mathbf{R}, \bar{t}). \end{aligned} \quad (\text{A18})$$

We can write the radial ($\alpha = R$) and the tangential ($\alpha = \theta$) flow velocities in the flowing form,

$$u_\alpha^h(\mathbf{R}, \bar{t}) = \frac{\hbar}{m} \frac{\text{Im}[\phi_h^*(\mathbf{R}, \bar{t}) \hat{\mathbf{e}}_\alpha \cdot \nabla \phi_h(\mathbf{R}, \bar{t})]}{|\phi_h(\mathbf{R}, \bar{t})|^2}. \quad (\text{A19})$$

Incorporating this expression, Eq. (A15) becomes,

$$\sum_{h \in T, a \in P} Y_{ha}^\alpha Y_{ha}^{\beta*} = \sum_{h \in T} \int d\mathbf{R} \tilde{g}(X') G_T(\tau) J_{\alpha\beta}^T(\mathbf{R}, \bar{t}). \quad (\text{A20})$$

Here, $J_{\alpha\beta}^T(\mathbf{R}, \bar{t})$ is given in Eq. (37), and $G_T(\tau)$ denotes the average memory kernel given by Eq. (A16), which is evaluated with the average value of the flow velocity of the hole states originating from the target. The second term on the right side of Eq. (34) is evaluated in a similar manner, and we obtain the expression given by Eq. (36) for the momentum diffusion coefficients.

Appendix B: Radial friction coefficient

In this Appendix, we discuss an analysis of the radial friction coefficient based on the mean-field solution of TDHF. The TDHF description contains the one-body dissipation of relative kinetic energy and the transfer of the relative angular momentum into the intrinsic degrees of freedom. The dominant mechanism for the one-body dissipation is nucleon exchange between projectile-like and target-like fragments. However, a microscopic derivation of the so-called window formula for the reduced friction coefficients from the TDHF approach is not trivial. Here, we consider the analogy with the random walk problem to deduce the reduced friction coefficients from the mean description of TDHF. By taking the ensemble average in Eq. (17), the mean evolution of the rate of change of the relative momentum is given by

$$\frac{\partial}{\partial t} \mathbf{P} = \int d\mathbf{r} g(x') \dot{x}' m \mathbf{j}(\mathbf{r}, t) + [\text{Potential terms}] + \mathbf{f}(t), \quad (\text{B1})$$

where $\mathbf{j}(\mathbf{r}, t) = \frac{\hbar}{m} \sum_h \text{Im}[\phi_h^*(\mathbf{r}, t) \nabla \phi_h(\mathbf{r}, t)]$. This equation is equivalent to the TDHF description of the relative momentum. The first and the second terms on the right hand side are the conservative forces on the relative motion due the motion of the window and the potential terms. In the last term $\mathbf{f}(t)$ represents the dynamical force due to nucleon exchange between the projectile- and target-like fragments with the radial and the tangential components,

$$f_\alpha(t) = \int d\mathbf{r} g(x') \sum_h \hat{e}_R \cdot (\mathbf{A}_{hh}^\alpha - \mathbf{B}_{hh}^\alpha) \quad (\text{B2})$$

Using the approximate result of Eq. (A17) in Appendix A, we can express the component of the dynamical force due to nucleon exchange as

$$f_\alpha(t) = -\frac{\hbar}{m} \int d\mathbf{r} g(x') \sum_h m u_\alpha^h(\mathbf{r}, t) \times \text{Im}[\phi_h^*(\mathbf{r}, t) \hat{e}_R \cdot \nabla \phi_h(\mathbf{r}, t)], \quad (\text{B3})$$

where the summation runs over the hole states originating from both projectile and target nuclei. The dynamical force involves both the conservative and dissipative forces. In order to infer the dissipative part of the dynamical force, we use the analogy to the Langevin description of the random walk problem. As seen in Eq. (36), the direct terms of the momentum

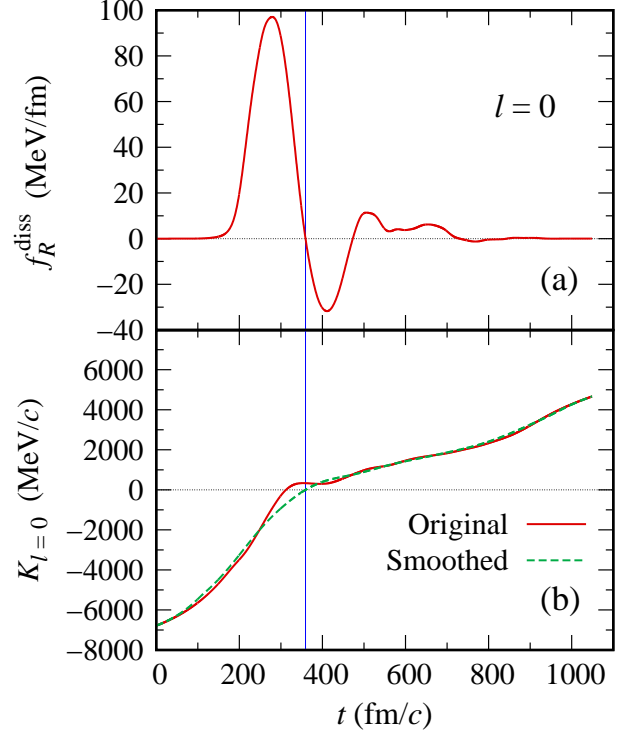


FIG. B1. The radial friction force $f_{l=0}^{\text{diss}}$ (a) and the radial momentum $K_{l=0}$ (b) are shown as a function of time for the central collision ($l = 0$). In panel (b), the original value of the radial momentum obtained from TDHF is shown by the solid line, while a smoothed curve is represented by the dashed line. The vertical line indicates the time at which $f_{l=0}^{\text{diss}}$ and the smoothed $K_{l=0}$ vanish.

diffusion coefficients are determined by the sum of nucleon fluxes that carry the product of momentum components from projectile to target and vice versa. In analogy to the description of the random walk, the components of the dissipative force are determined by the net momentum flux across the window as follows:

$$f_\alpha^{\text{diss}}(t) = -\frac{\hbar}{m} \int d\mathbf{r} g(x') \sum_{h \in P} m u_\alpha^h(\mathbf{r}, t) \times \left| \text{Im}[\phi_h^*(\mathbf{r}, t) \hat{e}_R \cdot \nabla \phi_h(\mathbf{r}, t)] \right| + \frac{\hbar}{m} \int d\mathbf{r} g(x') \sum_{h \in T} m u_\alpha^h(\mathbf{r}, t) \times \left| \text{Im}[\phi_h^*(\mathbf{r}, t) \hat{e}_R \cdot \nabla \phi_h(\mathbf{r}, t)] \right|. \quad (\text{B4})$$

Here, we express the net momentum flux as the difference of the momentum flux carried by the hole orbitals originating from the projectile and the momentum flux carried by the hole orbitals originating from the target. This approximate description may over estimate the net momentum flux, in particular in collisions at large impact parameters, and may require improvements. The quantity $|\text{Im}[\phi_h^*(\mathbf{r}, t) \hat{e}_R \cdot \nabla \phi_h(\mathbf{r}, t)]|$ represents the magnitude of the nucleon flux from one fragment to the other.

In this work, we consider the radial friction force and the reduced radial friction coefficient. In order to derive the expressions for the radial friction coefficient $\gamma_R(t, l)$ for collisions

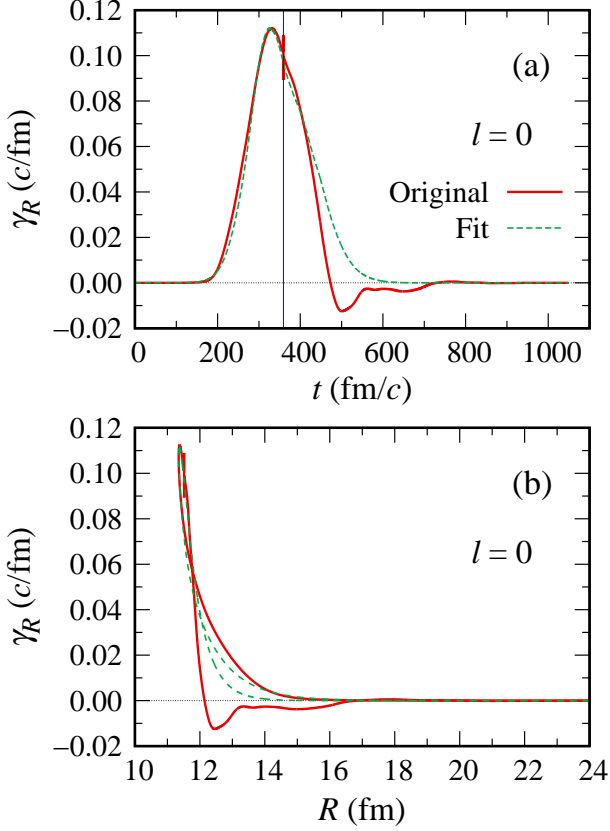


FIG. B2. The extracted reduced radial friction coefficient, $\gamma_R(t, l = 0) = -f_{l=0}^{\text{diss}}(t)/\bar{K}_{l=0}(t)$, is shown by the solid line for the central collision ($l = 0$), where $\bar{K}_{l=0}(t)$ is the smoothed radial momentum shown in Fig. B1(b) by the dashed line. In panel (a), it is shown as a function of time, while the same quantity is shown as a function of the relative distance in panel (b). The dashed line represents the parametrized function given by Eqs. (B7) and (B8).

with a range of initial angular momenta l , we assume the phenomenological expression for the radial dissipative force,

$$f_R^{\text{diss}}(t, l) = -\gamma_R(t, l)K_l(t), \quad (\text{B5})$$

where $K_l = \hat{e}_R \cdot \mathbf{P}_l$ is the radial component of the relative linear momentum. From this relation, in principle, it should be possible to deduce the radial friction coefficient for each value of the initial angular momentum l . In Fig. B1, we show the radial friction force in (a) and the radial momentum in (b) for the central collisions ($l = 0$) as a function of time. The radial momentum vanishes at the turning point which occurs at $t = 313$ fm/c (see Fig. B1(b), solid line). We expect that the radial friction force also vanishes at the turning point. However, we notice that the friction force vanishes at a slightly later time, $t = 360$ fm/c. The time shift may originate from the approximate expression of the friction force, Eq. (B4), which overestimates the net momentum flux across the window, and the shift becomes larger for increasing the orbital angular momentum.

In order to extract the radial friction coefficients for all values of the initial angular momentum l , we employ an approximate method as described below. In Fig. B1(b), we introduce a smoothing of the radial momentum so that the friction

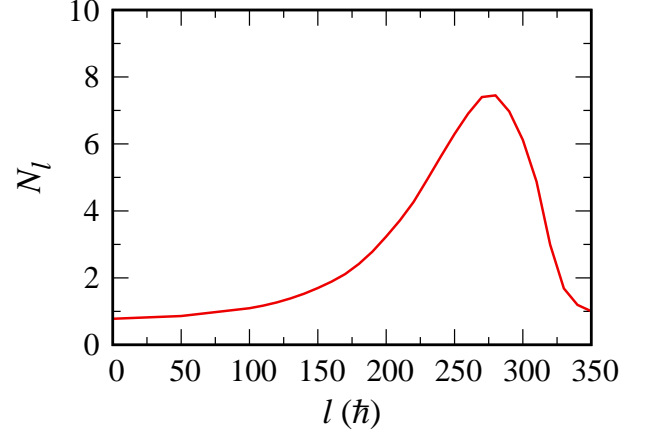


FIG. B3. The normalization coefficient N_l in Eq. (B9) is shown as a function of the initial orbital angular momentum l .

force and the radial momentum vanish at the same instant. The smoothed (averaged over a time interval of 220 fm/c) radial momentum, say $\bar{K}_{l=0}(t)$, is shown by the dashed line in Fig. B1(b), and the vertical line indicates the instant at which both the friction force and the radial momentum become vanishingly small. Then, we define the reduced friction coefficient for $l = 0$ as

$$\gamma_R(t, l = 0) = -\frac{f_R^{\text{diss}}(t, l = 0)}{\bar{K}_{l=0}(t)}. \quad (\text{B6})$$

Note that the phenomenological relation (B5) has been used.

In Fig. B2(a), we show the extracted friction coefficient according to Eq. (B6) in the central collision ($l = 0$) as a function of time (solid line). We find that dissipation occurs mainly during the incoming phase until the turning point at around $t = 360$ fm/c (indicated by a vertical line), and only a small fraction of dissipation takes place during the outgoing phase after the turning point until the separation of the fragments. We should thus ignore an unphysical negative tail after $t = 460$ fm/c. Figure B2(b) shows the friction coefficient γ_R in the central collision ($l = 0$) as a function of the relative distance $R(t)$. In this work, we parametrize the friction coefficient during the incoming phase by an exponential function as

$$\gamma_R^{\text{inc}}[R(t)] = c_1 \exp[-c_2(R(t) - c_3)], \quad (\text{B7})$$

with $c_1 = 9.97$ c/fm, $c_2 = 1.04$ fm⁻¹, and $c_3 = 6.86$ fm. The friction force reaches the maximum value at the minimum distance R_{min} . In the outgoing phase, from the minimum distance R_{min} to reseparation, we adopt another form with an exponential damping factor as

$$\gamma_R^{\text{out}}[R(t)] = \gamma_R^{\text{inc}}[R(t)] c_4 \exp[-c_5(R(t) - R_{\text{min}})], \quad (\text{B8})$$

where $c_4 = 1.96$ and $c_5 = 0.95$. Note that $c_4 > 1$ has been used, because the minimum distance is reached at $t = 313$ fm/c, while the obtained friction coefficient has a peak at slightly later time. We joint the two expressions for the incoming and outgoing phases smoothly around the turning

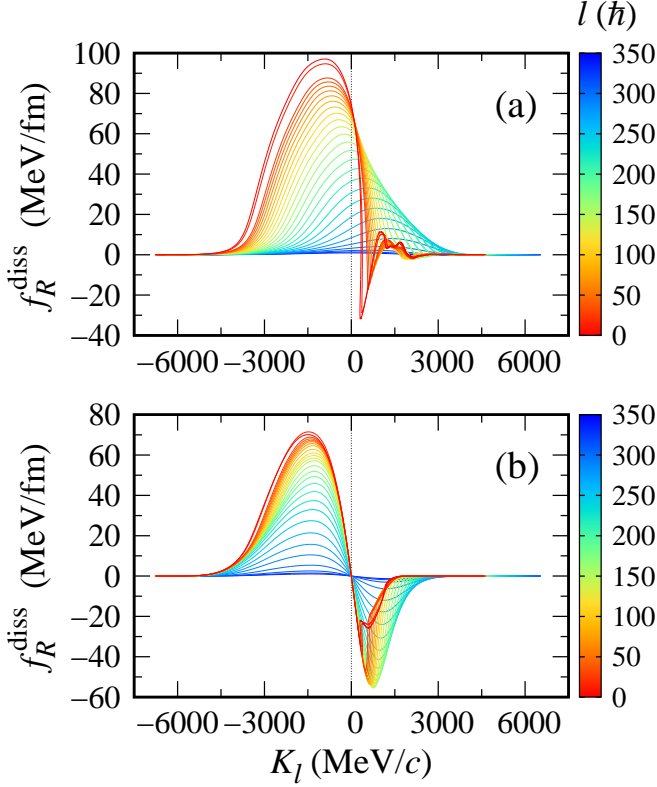


FIG. B4. The dissipative force F_l^{diss} is shown as a function of the radial linear momentum K_l for the $^{136}\text{Xe}+^{208}\text{Pb}$ reaction at $E_{c.m.} = 526$ MeV with a range of l values. Colors represent the value of the initial orbital angular momenta. (a) The dissipative force obtained with Eq. (B4) based on the single-particle orbitals in TDHF. (b) The reconstructed dissipative force according to the phenomenological expression, $F_l^{\text{diss}} = -\gamma_R K_l$, where γ_R here is expressed as the fitted function given by Eqs. (B7) and (B8).

point. Assuming that the friction coefficients scale with the relative distance for all initial angular momentum in a similar manner as for the central collision, we express the reduced radial friction coefficient for non-zero l values as,

$$\gamma_R(t, l) = N_l \gamma_R[R_l(t)]. \quad (\text{B9})$$

Here, $\gamma_R(R)$ is the friction coefficients given by Eqs. (B7) and (B8) extracted from the $l=0$ case as a function of the relative distance. The normalization factor N_l is determined by matching the dissipated energy with the mean TKEL calculated by TDHF for each initial angular momentum, i.e.,

$$E_l^{\text{diss}} = \int dt \gamma_R(t, l) \frac{K_l^2(t)}{\mu(t)} = E_{\text{kin}}^\infty(l). \quad (\text{B10})$$

In Fig. B3, we show the magnitude of the normalization constant C_l as a function of the initial orbital angular momentum l . Figure 2 in the main text presents the reduced radial friction coefficients determined in the manner outlined above as a function of time for typical initial orbital angular momenta.

In Fig. B4, we compare the original radial friction force as given by Eq. (B4) in panel (a) and the reconstructed radial friction force using the approximate treatment of Eq. (B9) in panel (b) as functions of the radial momentum for a range of

initial angular momenta l . It is visible that the original radial friction forces shown in (a) does not vanish at the turning point at which the radial momentum changes its sign. On the other hand, the reconstructed friction forces as functions of the radial momentum shown in (b) give rise to the expected behavior and provide a support for the reduced friction coefficients that we obtained using the approximate procedure.

Appendix C: Comparison with DD-TDHF

In this Appendix, we provide a supplemental analysis of the radial friction coefficient for head-on collision ($l=0$) based on an alternative approach, called dissipative-dynamics TDHF (DD-TDHF). The idea of DD-TDHF was first proposed in 1980 by Koonin [55], which was later tested for realistic applications by Lacroix in 2002 [56] and further applied by Washiyama *et al.* [57–59]. (See Ref. [60] for a short review.) Here let us succinctly recall the basic idea of DD-TDHF.

In DD-TDHF, we consider a mapping of TDHF dynamics onto a set of classical equations of motion:

$$\frac{dR}{dt} = \frac{P}{\mu}, \quad (\text{C1})$$

$$\frac{dP}{dt} = -\frac{dV_{\text{DD}}}{dR} - \frac{d}{dR} \left(\frac{P^2}{2\mu} \right) - \gamma_R P, \quad (\text{C2})$$

where $V_{\text{DD}}(R)$ and $\gamma_R(R)$ denote the nucleus-nucleus potential and the reduced radial friction coefficient, respectively, as a function of the relative distance R . A standard TDHF simulation provides time evolution of the relative distance $R(t)$, the relative linear momentum $P(t)$, and the reduced mass $\mu(t)$. Assuming that a slight change of collision energy does not affect the two unknown quantities, i.e., $V_{\text{DD}}(R)$ and $\gamma_R(R)$, one can solve the above equations for them. Namely, one finds:

$$\frac{dV_{\text{DD}}(R)}{dR} = \frac{\dot{R}_{\text{II}} \dot{P}_{\text{I}} - \dot{R}_{\text{I}} \dot{P}_{\text{II}}}{\dot{R}_{\text{I}} - \dot{R}_{\text{II}}} - \frac{1}{2} \frac{d\mu}{dR} \dot{R}_{\text{I}} \dot{R}_{\text{II}}, \quad (\text{C3})$$

$$\gamma_R(R) = \frac{\dot{P}_{\text{II}} - \dot{P}_{\text{I}}}{\dot{R}_{\text{I}} - \dot{R}_{\text{II}}} + \frac{1}{2} \frac{d\mu}{dR} (\dot{R}_{\text{I}} + \dot{R}_{\text{II}}), \quad (\text{C4})$$

where the subscript I (II) indicates that those quantities are associated with the TDHF trajectory I (II) at the collision energy E_{I} ($E_{\text{II}} = E_{\text{I}} + \Delta E$). In the analysis given below we set $\Delta E = 0.01 E_{\text{I}}$. Note that all quantities on the right hand side of Eqs. (C3) and (C4) should be evaluated at the same relative distance, $R = R_{\text{I}} = R_{\text{II}}$. The nucleus-nucleus potential $V_{\text{DD}}(R)$ can be obtained by a numerical integration of dV_{DD}/dR . We refer to Refs. [57–59] for details of numerical procedures.

In Fig. C1, the results obtained with the DD-TDHF method are presented. In Fig. C1(a), the extracted nucleus-nucleus potential $V_{\text{DD}}(R)$ is shown as a function of the relative distance (dashed line), in comparison with that obtained with the frozen-HF method [61]. In the latter approach, the nucleus-nucleus potential is evaluated simply by $V_{\text{FHF}}(R) = E[\rho_{\text{P}} + \rho_{\text{T}}](R) - E[\rho_{\text{P}}] - E[\rho_{\text{T}}]$, where $E[\rho]$ is the nuclear EDF and

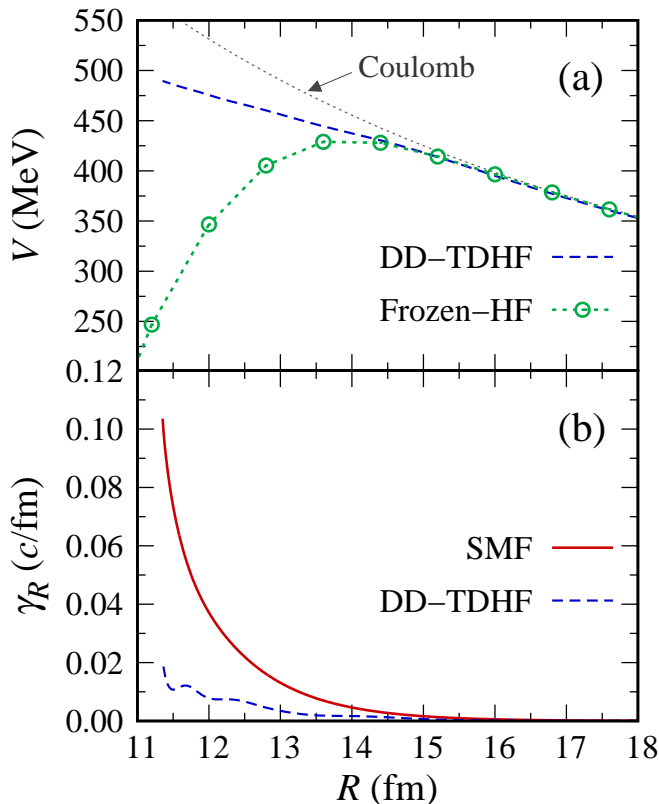


FIG. C1. (a) The nucleus-nucleus potential $V(R)$ is shown as a function of the relative distance R . The result obtained by the DD-TDHF method is shown by a dashed line. For comparison, the nucleus-nucleus potential obtained with the frozen-HF method and the point Coulomb potential are also shown by open circles connected with dotted lines and a dotted line, respectively. (b) The reduced radial friction coefficient $\gamma_R(R)$ for the incoming phase with $l = 0$ is shown as a function of the relative distance R . The result obtained with the SMF approach is shown by a solid line, while that of DD-TDHF is shown by a dashed line.

$\rho_{P(T)}$ denotes the ground-state density of the projectile (target) nucleus. It is to be reminded that the Pauli exclusion prin-

ciple among orbitals belonging to different nuclei is neglected in the frozen-HF potential, which can be taken into account by a density-constrained minimization technique [61]. Although we should thus expect an increase of the potential at short distances ($R \lesssim 14.5$ fm), we present V_{FHF} to have an estimate of the Coulomb barrier position. As can be seen from Fig. C1(a), we observe good agreement between V_{DD} and V_{FHF} at large distances ($R \gtrsim 15$ fm), as they should be. On the other hand, as the relative distance decreases, we observe a monotonic increase of V_{DD} , in contrast to the significant reduction in V_{FHF} . This is a characteristic behavior observed for heavy systems, which is related to the fusion hindrance phenomenon (see Ref. [59] for a detailed discussion).

In Fig. C1(b), we show the reduced radial friction coefficient $\gamma_R(R)$ for $l = 0$ as a function of the relative distance. The result based on the SMF approach is shown by a solid line, while the result of the DD-TDHF method is shown by a dashed line. Since the mapping onto the classical equations of motion breaks down around the turning point, we compare the results for the incoming phase only. From the figure, we find that the magnitude of the radial friction coefficient obtained with the SMF approach is larger than the DD-TDHF result roughly by factor of 4. We note that the radial friction coefficient in the SMF approach is consistent with the average TKEL in TDHF according to Eq. (B10).

In the SMF approach the friction coefficient has a microscopic origin associated with nucleon exchanges. On the other hand, in DD-TDHF the friction coefficient is extracted based solely on the macroscopic relative motion of the colliding nuclei. Based on the mapping of the classical equations of motion, the slowdown of the relative motion after collision (due to incompressible character of nuclear density and dinuclear shape formation) is mainly converted to the increase of the nucleus-nucleus potential [59]. However, the observed difference between SMF and DD-TDHF approaches may indicate that energy dissipation still takes place after the dinuclear system formation, because of the active nucleon exchanges between the reactants. It would be interesting to reexamine the origin of fusion hindrance in heavy systems based on the SMF approach.

-
- [1] S. Ayik, B. Shürmann, and W. Nörenberg, Microscopic transport theory of heavy-ion collisions, *Z. Phys. A* **277**, 299 (1976).
 - [2] D. Agassi, C.M. Ko, and H.A. Weidenmüller, Transport theory of deeply inelastic heavy-ion collisions based on a random-matrix model. i. Derivation of the transport equation, *Ann. Phys. (NY)* **107**, 140 (1977).
 - [3] J. Randrup, Nuclear one-body proximity friction, *Ann. Phys. (NY)* **112**, 356 (1978).
 - [4] J. Randrup, Theory of transfer-induced transport in nuclear collisions, *Nucl. Phys. A* **327**, 490 (1979).
 - [5] J.W. Negele, The mean-field theory of nuclear structure and dynamics, *Rev. Mod. Phys.* **54**, 913 (1982).
 - [6] C. Simenel, Nuclear quantum many-body dynamics, *Eur. Phys. J. A* **48**, 152 (2012).
 - [7] T. Nakatsukasa, K. Matsuyanagi, M. Matsuo, and K. Yabana, Time-dependent density-functional description of nuclear dynamics, *Rev. Mod. Phys.* **88**, 045004 (2016).
 - [8] C. Simenel and A.S. Umar, Heavy-ion collisions and fission dynamics with the time-dependent Hartree-Fock theory and its extensions, *Prog. Part. Nucl. Phys.* **103**, 19 (2018).
 - [9] P.D. Stevenson and M.C. Barton, Low-energy heavy-ion reactions and the Skyrme effective interaction, *Prog. Part. Nucl. Phys.* **104**, 142 (2019).
 - [10] K. Sekizawa, TDHF Theory and Its Extensions for Multinucleon Transfer Reactions: A Mini Review, *Front. Phys.* **7**, 20 (2019).
 - [11] C. Simenel, K. Godbey, and A.S. Umar, Timescales of Quantum Equilibration, Dissipation and Fluctuation in Nuclear Collisions, *Phys. Rev. Lett.* **124**, 212504 (2020).
 - [12] R. Balian and M. Vénéroni, Time-Dependent Variational Principle for Predicting the Expectation Value of an Observable, *Phys. Rev. Lett.* **47**, 1353 (1981); **47**, 1765 (1981).

- [13] R. Balian and M. Vénéroni, Fluctuations in a time-dependent mean-field approach, *Phys. Lett.* **B136**, 301 (1984).
- [14] R. Balian and M. Vénéroni, Time-dependent variational principle for the expectation value of an observable: Mean-field applications, *Ann. Phys. (NY)* **164**, 334 (1985).
- [15] J.M.A. Broomfield and P.D. Stevenson, Mass distributions beyond TDHF, in *FUSION08: New Aspects of Heavy Ion Collisions Near the Coulomb Barrier*, edited by K.E. Rehm, B.B. Back, H. Esbensen, and C.J. (Kim) Lister, AIP Conf. Proc. No. 1098 (AIP, New York, 2009), p. 133.
- [16] C. Simenel, Particle-Number Fluctuations and Correlations in Transfer Reactions Obtained Using the Balian-Vénéroni Variational Principle, *Phys. Rev. Lett.* **106**, 112502 (2011).
- [17] E. Williams, K. Sekizawa, D.J. Hinde, C. Simenel, M. Dasgupta, I.P. Carter, K.J. Cook, D.Y. Jeung, S.D. McNeil, C.S. Palshetkar, D.C. Rafferty, K. Ramachandran, and A. Wakhle, Exploring Zeptosecond Quantum Equilibration Dynamics: From Deep-Inelastic to Fusion-Fission Outcomes in $^{58}\text{Ni}+^{60}\text{Ni}$ Reactions, *Phys. Rev. Lett.* **120**, 022501 (2018).
- [18] K. Godbey, C. Simenel, and A.S. Umar, Microscopic predictions for production of neutron rich nuclei in the reaction $^{176}\text{Yb}+^{176}\text{Yb}$, *Phys. Rev. C* **101**, 034602 (2020).
- [19] J.B. Marston and S.E. Koonin, Mean-Field Calculations of Fluctuations in Nuclear Collisions, *Phys. Rev. Lett.* **54**, 1139 (1985).
- [20] S. Ayik, A stochastic mean-field approach for nuclear dynamics, *Phys. Lett.* **B658**, 174 (2008).
- [21] D. Lacroix and S. Ayik, Stochastic quantum dynamics beyond mean field, *Eur. Phys. J. A* **50**, 95 (2014).
- [22] F.-S. Zhang, C. Li, L. Zhu, and P. Wen, Production cross sections for exotic nuclei with multinucleon transfer reactions, *Front. Phys.* **13**, 132113 (2018).
- [23] G.G. Adamian, N.V. Antonenko, A. Diaz-Torres, and S. Heinz, How to extend the chart of nuclides?, *Eur. Phys. J. A* **56**, 47 (2020).
- [24] S. Ayik, O. Yilmaz, B. Yilmaz, and A.S. Umar, Quantal nucleon diffusion: Central collisions of symmetric nuclei, *Phys. Rev. C* **94**, 044624 (2016).
- [25] S. Ayik, B. Yilmaz, O. Yilmaz, A.S. Umar, and G. Turan, Multinucleon transfer in central collisions of $^{238}\text{U}+^{238}\text{U}$, *Phys. Rev. C* **96**, 024611 (2017).
- [26] S. Ayik, B. Yilmaz, O. Yilmaz, and A.S. Umar, Quantal diffusion description of multinucleon transfers in heavy-ion collisions, *Phys. Rev. C* **97**, 054618 (2018).
- [27] B. Yilmaz, S. Ayik, O. Yilmaz, and A.S. Umar, Multinucleon transfer in $^{58}\text{Ni}+^{60}\text{Ni}$ and $^{60}\text{Ni}+^{60}\text{Ni}$ in a stochastic mean-field approach, *Phys. Rev. C* **98**, 034604 (2018).
- [28] S. Ayik, B. Yilmaz, O. Yilmaz, and A.S. Umar, Quantal diffusion approach for multinucleon transfers in Xe + Pb collisions, *Phys. Rev. C* **100**, 014609 (2019).
- [29] S. Ayik, O. Yilmaz, B. Yilmaz, and A.S. Umar, Heavy-isotope production in $^{136}\text{Xe}+^{208}\text{Pb}$ collisions at $E_{c.m.} = 514$ MeV, *Phys. Rev. C* **100**, 044614 (2019).
- [30] O. Yilmaz, G. Turan, and B. Yilmaz, Quasi-fission and fusion-fission reactions in $^{48}\text{Ca}+^{208}\text{Pb}$ collisions at $E_{c.m.} = 190$ MeV, *Eur. Phys. J. A* **56**, 37 (2020).
- [31] K. Sekizawa and S. Ayik, Quantal diffusion approach for multinucleon transfer processes in the $^{58,64}\text{Ni}+^{208}\text{Pb}$ reactions: Toward the production of unknown neutron-rich nuclei, *Phys. Rev. C* **102**, 014620 (2020).
- [32] Y. Tanimura, D. Lacroix, and S. Ayik, Microscopic Phase-Space Exploration Modeling of ^{258}Fm Spontaneous Fission, *Phys. Rev. Lett.* **118**, 152501 (2017); *ibid.*, **121**, 059902(E) (2018).
- [33] E.M. Kozulin, E. Vardaci, G.N. Knyazheva, A.A. Bogachev, S.N. Dmitriev, I.M. Itkis, M.G. Itkis, A.G. Knyazev, T.A. Loktev, K.V. Novikov, E.A. Razinkov, O.V. Rudakov, S.V. Smirnov, W. Trzaska, and V.I. Zagrebaev, Mass distributions of the system $^{136}\text{Xe}+^{208}\text{Pb}$ at laboratory energies around the Coulomb barrier: A candidate reaction for the production of neutron-rich nuclei at $N = 126$, *Phys. Rev. C* **86**, 044611 (2012).
- [34] J.S. Barrett, W. Loveland, R. Yanez, S. Zhu, A.D. Ayangeakaa, M.P. Carpenter, J.P. Greene, R.V.F. Janssens, T. Lauritsen, E.A. McCutchan, A.A. Sonzogni, C.J. Chiara, J.L. Harker, and W.B. Walters, $^{136}\text{Xe}+^{208}\text{Pb}$ reaction: A test of models of multinucleon transfer reactions, *Phys. Rev. C* **91**, 064615 (2015).
- [35] A. Vogt *et al.*, Light and heavy transfer products in $^{136}\text{Xe}+^{238}\text{U}$ multinucleon transfer reactions, *Phys. Rev. C* **92**, 024619 (2015).
- [36] Y.X. Watanabe, Y.H. Kim, S.C. Jeong, Y. Hirayama, N. Imai, H. Ishiyama, H.S. Jung, H. Miyatake, S. Choi, J.S. Song, E. Clement, G. de France, A. Navin, M. Rejmund, C. Schmitt, G. Pollarolo, L. Corradi, E. Fioretto, D. Montanari, M. Niikura, D. Suzuki, H. Nishibata, and J. Takatsu, Pathway for the Production of Neutron-Rich Isotopes around the $N = 126$ Shell Closure, *Phys. Rev. Lett.* **115**, 172503 (2015).
- [37] T. Welsh, W. Loveland, R. Yanez, J.S. Barrett, E.A. McCutchan, A.A. Sonzogni, T. Johnson, S. Zhu, J.P. Greene, A.D. Ayangeakaa, M.P. Carpenter, T. Lauritsen, J.L. Harker, W.B. Walters, B.M.S. Amro, and P. Copp, Modeling multinucleon transfer in symmetric collisions of massive nuclei, *Phys. Lett.* **B771**, 119 (2017).
- [38] V.V. Desai, W. Loveland, K. McCaleb, R. Yanez, G. Lane, S.S. Hota, M.W. Reed, H. Watanabe, S. Zhu, K. Auranen, A.D. Ayangeakaa, M.P. Carpenter, J.P. Greene, F.G. Kondev, D. Seweryniak, R.V.F. Janssens, and P.A. Copp, The $^{136}\text{Xe}+^{198}\text{Pt}$ reaction: A test of models of multi-nucleon transfer reactions, *Phys. Rev. C* **99**, 044604 (2019).
- [39] V.V. Desai, A. Pica, W. Loveland, J.S. Barrett, E.A. McCutchan, S. Zhu, A.D. Ayangeakaa, M.P. Carpenter, J.P. Greene, T. Lauritsen, R.V.F. Janssens, B.M.S. Amro, and W.B. Walters, Multinucleon transfer in the interaction of 977 MeV and 1143 MeV ^{204}Hg with ^{208}Pb , *Phys. Rev. C* **101**, 034612 (2020).
- [40] V.V. Desai, W. Loveland, R. Yanez, G. Lane, S. Zhu, A.D. Ayangeakaa, J.P. Greene, F.G. Kondev, R.V.F. Janssens, and P.A. Copp, The $^{136}\text{Xe}+^{198}\text{Pt}$ reaction: a detailed re-examination, *Eur. Phys. J. A* **56**, 150 (2020).
- [41] C.W. Gardiner, *Quantum Noise* (Springer-Verlag, Berlin, 1991).
- [42] U. Weiss, *Quantum Dissipative Systems*, 2nd ed. (World Scientific, Singapore, 1999).
- [43] A.C. Merchant and W. Nörenberg, Microscopic Transport Theory of Heavy-Ion Collisions, *Z. Phys. A* **308**, 315 (1982).
- [44] W.U. Schröder, J.R. Huizenga, and J. Randrup, Correlated mass and charge transport induced by statistical nucleon exchange in damped nuclear reactions, *Phys. Lett.* **B98**, 355 (1981).
- [45] H. Risken and T. Frank, *The Fokker-Planck Equation* (Springer-Verlag, Berlin, 1996).
- [46] K. Gottfried, *Quantum Mechanics* (W.A. Benjamin Inc., New York, 1966).
- [47] K. Sekizawa and K. Yabana, Time-dependent Hartree-Fock calculations for multinucleon transfer processes in $^{40,48}\text{Ca}+^{124}\text{Sn}$, $^{40}\text{Ca}+^{208}\text{Pb}$, and $^{58}\text{Ni}+^{208}\text{Pb}$ reactions, *Phys. Rev. C* **88**, 014614 (2013); **93**, 029902(E) (2016).
- [48] K. Sekizawa and K. Yabana, Particle-number projection method in time-dependent Hartree-Fock theory, *Phys. Rev. C* **90**, 064614 (2014).
- [49] Sonika, B.J. Roy, A. Parmar, U.K. Pal, H. Kumawat, V. Jha, S.K. Pandit, V.V. Parkar, K. Ramachandran, K. Mahata, A. Pal, S. Santra, A.K. Mohanty, and K. Sekizawa, Multinucleon trans-

- fer study in $^{206}\text{Pb}(^{18}\text{O}, x)$ at energies above the Coulomb barrier, *Phys. Rev. C* **92**, 024603 (2015).
- [50] K. Sekizawa and K. Yabana, Time-dependent Hartree-Fock calculations for multinucleon transfer and quasifission processes in the $^{64}\text{Ni}+^{238}\text{U}$ reaction, *Phys. Rev. C* **93**, 054616 (2016).
- [51] K. Sekizawa, Enhanced nucleon transfer in tip collisions of $^{238}\text{U}+^{124}\text{Sn}$, *Phys. Rev. C* **96**, 041601(R) (2017).
- [52] B.J. Roy, Y. Sawant, P. Patwari, S. Santra, A. Pal, A. Kundu, D. Chattopadhyay, V. Jha, S.K. Pandit, V.V. Parkar, K. Ramachandran, K. Mahata, B.K. Nayak, A. Saxena, S. Kailas, T.N. Nag, R.N. Sahoo, P.P. Singh, and K. Sekizawa, Deep-inelastic multinucleon transfer processes in the $^{16}\text{O}+^{27}\text{Al}$ reaction, *Phys. Rev. C* **97**, 034603 (2018).
- [53] K. Sekizawa, Microscopic description of production cross sections including deexcitation effects, *Phys. Rev. C* **96**, 014615 (2017).
- [54] H. Mori, Transport, Collective Motion, and Brownian Motion, *Prog. Theor. Phys.* **33**, 423 (1965).
- [55] S.E. Koonin, The Time-Dependent Hartree-Fock Description of Heavy-Ion Collisions, *Prog. Part. Nucl. Phys.* **4**, 283 (1980).
- [56] D. Lacroix, From microscopic to macroscopic dynamics in mean-field theory: effect of neutron skin on fusion barrier and dissipation, arXiv:nucl-th/0202063 (2002).
- [57] K. Washiyama and D. Lacroix, Energy dependence of the nucleus-nucleus potential close to the Coulomb barrier, *Phys. Rev. C* **78**, 024610 (2008).
- [58] K. Washiyama, D. Lacroix, and S. Ayik, One-body energy dissipation in fusion reactions from mean-field theory, *Phys. Rev. C* **79**, 024609 (2009).
- [59] K. Washiyama, Microscopic analysis of fusion hindrance in heavy nuclear systems, *Phys. Rev. C* **91**, 064607 (2015).
- [60] K. Washiyama and K. Sekizawa, TDHF and a Macroscopic Aspect of Low-Energy Nuclear Reactions, *Front. Phys.* **8**, 93 (2020).
- [61] C. Simenel, A.S. Umar, K. Godbey, M. Dasgupta, and D.J. Hinde, How the Pauli exclusion principle affects fusion of atomic nuclei, *Phys. Rev. C* **95**, 031601(R) (2017).